EUROPEAN LABORATORY FOR PARTICLE PHYSICS

CERN-EP/99-076
3rd June 1999

Total Hadronic Cross-Section of Photon-Photon Interactions at LEP

The OPAL Collaboration

Abstract

The total hadronic cross-section $\sigma_{\gamma\gamma}(W)$ for the interaction of real photons, $\gamma\gamma \to$ hadrons, is measured for $\gamma\gamma$ centre-of-mass energies $10 \leq W \leq 110$ GeV. The cross-section is extracted from a measurement of the process $e^+e^- \to e^+e^-\gamma^*\gamma^* \to e^+e^-$ + hadrons, using a luminosity function for the photon flux together with form factors for extrapolating to real photons ($Q^2 = 0$ GeV^2). The data were taken with the OPAL detector at LEP at e^+e^- centre-of-mass energies $\sqrt{s}_{ee} = 161, 172$ and 183 GeV. The cross-section $\sigma_{\gamma\gamma}(W)$ is compared with Regge factorisation and with the energy dependence observed in γp and pp interactions. The data are also compared to models which predict a faster rise of $\sigma_{\gamma\gamma}(W)$ compared to γp and pp interactions due to additional hard $\gamma\gamma$ interactions not present in hadronic collisions.

(To be submitted to European Physical Journal C)

The OPAL Collaboration

G. Abbiendi[2], K. Ackerstaff[8], G. Alexander[23], J. Allison[16], N. Altekamp[5], K.J. Anderson[9], S. Anderson[12], S. Arcelli[17], S. Asai[24], S.F. Ashby[1], D. Axen[29], G. Azuelos[18,a], A.H. Ball[8], E. Barberio[8], T. Barillari[2], R.J. Barlow[16], J.R. Batley[5], S. Baumann[3], J. Bechtluft[14], T. Behnke[27], K.W. Bell[20], G. Bella[23], A. Bellerive[9], S. Bentvelsen[8], S. Bethke[14], S. Betts[15], O. Biebel[14], A. Biguzzi[5], I.J. Bloodworth[1], P. Bock[11], J. Böhme[14], D. Bonacorsi[2], M. Boutemeur[33], S. Braibant[8], P. Bright-Thomas[1], L. Brigliadori[2], R.M. Brown[20], H.J. Burckhart[8], P. Capiluppi[2], R.K. Carnegie[6], A.A. Carter[13], J.R. Carter[5], C.Y. Chang[17], D.G. Charlton[1,b], D. Chrisman[4], C. Ciocca[2], P.E.L. Clarke[15], E. Clay[15], I. Cohen[23], J.E. Conboy[15], O.C. Cooke[8], J. Couchman[15], C. Couyoumtzelis[13], R.L. Coxe[9], M. Cuffiani[2], S. Dado[22], G.M. Dallavalle[2], R. Davis[30], S. De Jong[12], A. de Roeck[8], P. Dervan[15], K. Desch[27], B. Dienes[32,h], M.S. Dixit[7], J. Dubbert[33], E. Duchovni[26], G. Duckeck[33], I.P. Duerdoth[16], P.G. Estabrooks[6], E. Etzion[23], F. Fabbri[2], A. Fanfani[2], M. Fanti[2], A.A. Faust[30], L. Feld[10], F. Fiedler[27], M. Fierro[2], I. Fleck[10], A. Frey[8], A. Fürtjes[8], D.I. Futyan[16], P. Gagnon[7], J.W. Gary[4], G. Gaycken[27], C. Geich-Gimbel[3], G. Giacomelli[2], P. Giacomelli[2], V. Gibson[5], W.R. Gibson[13], D.M. Gingrich[30,a], D. Glenzinski[9], J. Goldberg[22], W. Gorn[4], C. Grandi[2], K. Graham[28], E. Gross[26], J. Grunhaus[23], M. Gruwé[27], C. Hajdu[31] G.G. Hanson[12], M. Hansroul[8], M. Hapke[13], K. Harder[27], A. Harel[22], C.K. Hargrove[7], M. Harin-Dirac[4], M. Hauschild[8], C.M. Hawkes[1], R. Hawkings[27], R.J. Hemingway[6], G. Herten[10], R.D. Heuer[27], M.D. Hildreth[8], J.C. Hill[5], P.R. Hobson[25], A. Hocker[9], K. Hoffman[8], R.J. Homer[1], A.K. Honma[28,a], D. Horváth[31,c], K.R. Hossain[30], R. Howard[29], P. Hüntemeyer[27], P. Igo-Kemenes[11], D.C. Imrie[25], K. Ishii[24], F.R. Jacob[20], A. Jawahery[17], H. Jeremie[18], M. Jimack[1], C.R. Jones[5], P. Jovanovic[1], T.R. Junk[6], N. Kanaya[24], J. Kanzaki[24], D. Karlen[6], V. Kartvelishvili[16], K. Kawagoe[24], T. Kawamoto[24], P.I. Kayal[30], R.K. Keeler[28], R.G. Kellogg[17], B.W. Kennedy[20], D.H. Kim[19], A. Klier[26], T. Kobayashi[24], M. Kobel[3,d], T.P. Kokott[3], M. Kolrep[10], S. Komamiya[24], R.V. Kowalewski[28], T. Kress[4], P. Krieger[6], J. von Krogh[11], T. Kuhl[3], P. Kyberd[13], G.D. Lafferty[16], H. Landsman[22], D. Lanske[14], J. Lauber[15], I. Lawson[28], J.G. Layter[4], D. Lellouch[26], J. Letts[12], L. Levinson[26], R. Liebisch[11], B. List[8], C. Littlewood[5], A.W. Lloyd[1], S.L. Lloyd[13], F.K. Loebinger[16], G.D. Long[28], M.J. Losty[7], J. Lu[29], J. Ludwig[10], D. Liu[12], A. Macchiolo[18], A. Macpherson[30], W. Mader[3], M. Mannelli[8], S. Marcellini[2], A.J. Martin[13], J.P. Martin[18], G. Martinez[17], T. Mashimo[24], P. Mättig[26], W.J. McDonald[30], J. McKenna[29], E.A. Mckigney[15], T.J. McMahon[1], R.A. McPherson[28], F. Meijers[8], P. Mendez-Lorenzo[33], F.S. Merritt[9], H. Mes[7], A. Michelini[2], S. Mihara[24], G. Mikenberg[26], D.J. Miller[15], W. Mohr[10], A. Montanari[2], T. Mori[24], K. Nagai[8], I. Nakamura[24], H.A. Neal[12,g], R. Nisius[8], S.W. O'Neale[1], F.G. Oakham[7], F. Odorici[2], H.O. Ogren[12], A. Okpara[11], M.J. Oreglia[9], S. Orito[24], G. Pásztor[31], J.R. Pater[16], G.N. Patrick[20], J. Patt[10], R. Perez-Ochoa[8], S. Petzold[27], P. Pfeifenschneider[14], J.E. Pilcher[9], J. Pinfold[30], D.E. Plane[8], P. Poffenberger[28], B. Poli[2], J. Polok[8], M. Przybycień[8,e], A. Quadt[8], C. Rembser[8], H. Rick[8], S. Robertson[28], S.A. Robins[22], N. Rodning[30], J.M. Roney[28], S. Rosati[3], K. Roscoe[16], A.M. Rossi[2], Y. Rozen[22], K. Runge[10], O. Runolfsson[8], D.R. Rust[12], K. Sachs[10], T. Saeki[24], O. Sahr[33], W.M. Sang[25], E.K.G. Sarkisyan[23], C. Sbarra[29], A.D. Schaile[33], O. Schaile[33], P. Scharff-Hansen[8], J. Schieck[11], S. Schmitt[11], A. Schöning[8], M. Schröder[8], M. Schumacher[3], C. Schwick[8], W.G. Scott[20], R. Seuster[14], T.G. Shears[8], B.C. Shen[4], C.H. Shepherd-Themistocleous[5], P. Sherwood[15], G.P. Siroli[2], A. Sittler[27], A. Skuja[17], A.M. Smith[8], G.A. Snow[17], R. Sobie[28], S. Söldner-Rembold[10,f], S. Spagnolo[20], M. Sproston[20], A. Stahl[3], K. Stephens[16], J. Steuerer[27], K. Stoll[10], D. Strom[19], R. Ströhmer[33], B. Surrow[8], S.D. Talbot[1], P. Taras[18], S. Tarem[22], R. Teuscher[9], M. Thiergen[10], J. Thomas[15],

M.A. Thomson[8], E. Torrence[8], S. Towers[6], I. Trigger[18], Z. Trócsányi[32], E. Tsur[23], M.F. Turner-Watson[1], I. Ueda[24], R. Van Kooten[12], P. Vannerem[10], M. Verzocchi[8], H. Voss[3], F. Wäckerle[10], A. Wagner[27], C.P. Ward[5], D.R. Ward[5], P.M. Watkins[1], A.T. Watson[1], N.K. Watson[1], P.S. Wells[8], N. Wermes[3], D. Wetterling[11] J.S. White[6], G.W. Wilson[16], J.A. Wilson[1], T.R. Wyatt[16], S. Yamashita[24], V. Zacek[18], D. Zer-Zion[8]

[1]School of Physics and Astronomy, University of Birmingham, Birmingham B15 2TT, UK
[2]Dipartimento di Fisica dell' Università di Bologna and INFN, I-40126 Bologna, Italy
[3]Physikalisches Institut, Universität Bonn, D-53115 Bonn, Germany
[4]Department of Physics, University of California, Riverside CA 92521, USA
[5]Cavendish Laboratory, Cambridge CB3 0HE, UK
[6]Ottawa-Carleton Institute for Physics, Department of Physics, Carleton University, Ottawa, Ontario K1S 5B6, Canada
[7]Centre for Research in Particle Physics, Carleton University, Ottawa, Ontario K1S 5B6, Canada
[8]CERN, European Organisation for Particle Physics, CH-1211 Geneva 23, Switzerland
[9]Enrico Fermi Institute and Department of Physics, University of Chicago, Chicago IL 60637, USA
[10]Fakultät für Physik, Albert Ludwigs Universität, D-79104 Freiburg, Germany
[11]Physikalisches Institut, Universität Heidelberg, D-69120 Heidelberg, Germany
[12]Indiana University, Department of Physics, Swain Hall West 117, Bloomington IN 47405, USA
[13]Queen Mary and Westfield College, University of London, London E1 4NS, UK
[14]Technische Hochschule Aachen, III Physikalisches Institut, Sommerfeldstrasse 26-28, D-52056 Aachen, Germany
[15]University College London, London WC1E 6BT, UK
[16]Department of Physics, Schuster Laboratory, The University, Manchester M13 9PL, UK
[17]Department of Physics, University of Maryland, College Park, MD 20742, USA
[18]Laboratoire de Physique Nucléaire, Université de Montréal, Montréal, Quebec H3C 3J7, Canada
[19]University of Oregon, Department of Physics, Eugene OR 97403, USA
[20]CLRC Rutherford Appleton Laboratory, Chilton, Didcot, Oxfordshire OX11 0QX, UK
[22]Department of Physics, Technion-Israel Institute of Technology, Haifa 32000, Israel
[23]Department of Physics and Astronomy, Tel Aviv University, Tel Aviv 69978, Israel
[24]International Centre for Elementary Particle Physics and Department of Physics, University of Tokyo, Tokyo 113-0033, and Kobe University, Kobe 657-8501, Japan
[25]Institute of Physical and Environmental Sciences, Brunel University, Uxbridge, Middlesex UB8 3PH, UK
[26]Particle Physics Department, Weizmann Institute of Science, Rehovot 76100, Israel
[27]Universität Hamburg/DESY, II Institut für Experimental Physik, Notkestrasse 85, D-22607 Hamburg, Germany
[28]University of Victoria, Department of Physics, P O Box 3055, Victoria BC V8W 3P6, Canada
[29]University of British Columbia, Department of Physics, Vancouver BC V6T 1Z1, Canada
[30]University of Alberta, Department of Physics, Edmonton AB T6G 2J1, Canada
[31]Research Institute for Particle and Nuclear Physics, H-1525 Budapest, P O Box 49, Hungary
[32]Institute of Nuclear Research, H-4001 Debrecen, P O Box 51, Hungary

[33]Ludwigs-Maximilians-Universität München, Sektion Physik, Am Coulombwall 1, D-85748 Garching, Germany

[a] and at TRIUMF, Vancouver, Canada V6T 2A3
[b] and Royal Society University Research Fellow
[c] and Institute of Nuclear Research, Debrecen, Hungary
[d] on leave of absence from the University of Freiburg
[e] and University of Mining and Metallurgy, Cracow
[f] and Heisenberg Fellow
[g] now at Yale University, Dept of Physics, New Haven, USA
[h] and Depart of Experimental Physics, Lajos Kossuth University, Debrecen, Hungary.

1 Introduction

At high $\gamma\gamma$ centre-of-mass energies $W = \sqrt{s}_{\gamma\gamma}$, the total hadronic cross-section $\sigma_{\gamma\gamma}$ for the production of hadrons in the interaction of two real photons is expected to be dominated by interactions where the photons have fluctuated into a hadronic state. Measuring the $\sqrt{s}_{\gamma\gamma}$ dependence of $\sigma_{\gamma\gamma}$ should therefore improve our understanding of the hadronic nature of the photon and the universal high-energy behaviour of total hadronic cross-sections.

Before data from LEP became available, the total hadronic $\gamma\gamma$ cross-section had only been measured for $\gamma\gamma$ centre-of-mass energies W below 20 GeV by PLUTO [1], TPC/2γ [2], PEP/2γ [3] and the MD1 experiment [4], in a kinematic region where the expected high-energy rise of the total cross-section could not have been observed. Using LEP data taken at e^+e^- centre-of-mass energies $\sqrt{s}_{ee} = 130 - 161$ GeV, L3 [5] has demonstrated that the total hadronic $\gamma\gamma$ cross-section in the range $5 \leq W \leq 75$ GeV is consistent with the universal Regge behaviour of total cross-sections.

Processes with a pointlike coupling of the photon to quarks are absent in hadron-hadron collisions. This additional hard component in photon interactions is therefore expected to lead to a different energy dependence of the total cross-section for photon-induced interactions in comparison to hadron-hadron scattering. Models [6, 7] based on perturbative Quantum Chromodynamics (pQCD) encompass this by including additional photon interactions, usually denoted "direct" and "anomalous", in addition to the interactions which are described by the Vector Meson Dominance model (VMD). In VMD models, the photon fluctuates into a bound state vector meson. In Regge models, a different energy dependence of the cross-section can be obtained either by universality breaking effects or by introducing an additional hard pomeron [8]. Thus far no sign of such a different energy dependence has been experimentally established in comparison of the total γp cross-section measured by the HERA experiments [9, 10] with total pp cross-sections. Any such effect would be expected to be more pronounced in $\gamma\gamma$ interactions, since here one has two photons in the initial state.

In this paper, we present a measurement of the total hadronic $\gamma\gamma$ cross-section in the range $10 < W < 110$ GeV using data taken by the OPAL detector at LEP at $\sqrt{s}_{ee} = 161$,

172 and 183 GeV. The integrated luminosities are 9.9, 10.0 and 54.4 pb^{-1}, respectively. At these energies above the Z^0 resonance, hadron production is dominated by photon-photon collisions and background from other processes, e.g. $\mathrm{e}^+\mathrm{e}^-$ annihilation, is expected to be small. The photon-photon events are selected by a series of cuts intended to exclude backgrounds, especially from the $\mathrm{e}^+\mathrm{e}^-$ annihilation and $\gamma\gamma \to \ell^+\ell^-$ channels ($\ell \in \{\mathrm{e}, \mu, \tau\}$). In addition, an anti-tagging condition is applied, requiring that no scattered electron[1] was detected. Most of the photons therefore carry only a small negative four-momentum squared, Q^2, and can be considered to be quasi-real ($Q^2 \approx 0$ GeV^2). The differential cross-section $\mathrm{d}\sigma/\mathrm{d}W$ is measured for the process $\mathrm{e}^+\mathrm{e}^- \to \mathrm{e}^+\mathrm{e}^-$ + hadrons, where W is the invariant mass of the hadronic system. From this cross-section the total hadronic cross-section $\sigma_{\gamma\gamma}(W)$ for the interaction of real photons, $\gamma\gamma \to$ hadrons, is extracted as a function of W, using a luminosity function for the photon flux and form factors for the extrapolation to $Q^2 = 0$ GeV^2.

2 The OPAL detector

A detailed description of the OPAL detector can be found in Ref. [11], and therefore only a brief account of the main features relevant to the present analysis will be given here.

The central tracking system, covering the polar angle range $|\cos\theta| < 0.73$, is located inside a solenoidal magnet which provides a uniform magnetic field of 0.435 T along the beam axis[2]. The magnet is surrounded in the barrel region ($|\cos\theta| < 0.82$) by a lead glass electromagnetic calorimeter (ECAL) and a hadronic sampling calorimeter (HCAL). Outside the HCAL, the detector is surrounded by muon chambers. There are similar layers of detectors in the endcaps ($0.82 < |\cos\theta| < 0.98$). The small-angle region from 47 to 140 mrad around the beam pipe on both sides of the interaction point is covered by the forward detectors (FD) and the region from 25 to 59 mrad by the silicon-tungsten luminometers (SW). From 1996 onwards, relevant to the data presented in this paper, the lower boundary of the SW acceptance has been increased to 33 mrad following the installation of a low-angle shield to protect the central detector against synchrotron radiation due to the increased LEP $\mathrm{e}^+\mathrm{e}^-$ beam energies.

Starting with the innermost components, the tracking system consists of a high precision silicon microvertex detector, a vertex drift chamber, a large volume jet chamber with 159 layers of axial anode wires and a set of z chambers measuring the track coordinates along the beam direction. The transverse momenta p_T of tracks are measured with a precision parametrised by $\sigma_{p_\mathrm{T}}/p_\mathrm{T} = \sqrt{0.02^2 + (0.0015 \cdot p_\mathrm{T})^2}$ (p_T in GeV/c) in the central region. In this paper, "transverse" is always defined with respect to the z axis. The jet chamber also provides measurements of track energy loss, $\mathrm{d}E/\mathrm{d}x$, which are used for particle identification [11].

The barrel and endcap sections of the ECAL are both constructed from lead-glass blocks, with a depth of 24.6 radiation lengths in the barrel region and more than 22 radiation lengths in the endcaps. The FD consist of cylindrical lead-scintillator calorimeters with a depth of 24 radiation lengths divided azimuthally into 16 segments. The electromagnetic energy resolution

[1] Positrons are also referred to as electrons

[2] In the OPAL coordinate system the z axis points in the direction of the e^- beam. The polar angle θ, the azimuthal angle ϕ and the radius r denote the usual spherical coordinates.

is about $18\%/\sqrt{E}$, where E is the energy in GeV. The SW detectors [12] each consist of 19 layers of silicon interleaved with 18 layers of tungsten, corresponding to a total of 22 radiation lengths. Each silicon layer consists of 16 wedge shaped silicon detectors. The electromagnetic energy resolution is about $25\%/\sqrt{E}$ (E in GeV).

3 Kinematics

A schematic diagram of the two-photon process is shown in Fig. 1. The kinematics of the process $e^+e^- \to e^+e^- +$ hadrons at a given $\sqrt{s}_{ee}$ can be described by the negative square of the four-momentum transfers, $Q_i^2 = -q_i^2$, carried by the two ($i = 1, 2$) incoming virtual photons (γ^*) and by the square of the invariant mass of the hadronic final state, $W^2 = s_{\gamma\gamma} = (q_1 + q_2)^2$. The four-momenta of the electrons before and after the interaction are denoted by p_i and p_i', respectively. Each Q_i^2 is related to the electron scattering angle θ_i' relative to the beam direction by

$$Q_i^2 = -(p_i - p_i')^2 \approx 2E_iE_i'(1 - \cos\theta_i'), \tag{1}$$

where E_i and E_i' are the energies of the beam electron and the scattered electron, respectively. Events are only included in the analysis if they do not contain scattered electrons (either single-tagged or double-tagged events). This anti-tagging condition defines an effective upper limit on the values of Q_i^2 for both photons. This condition is either met if the scattering angle θ_i' of the electron is less than 33 mrad, defined by the angle between the beam axis and the inner edge of the acceptance of the SW detector, or if the energy of the scattered electron is smaller than the minimum energy of 20 GeV required for the tagged electron in SW or 40 GeV in FD.

4 Event selection

Two-photon events are selected with the following set of cuts:

- The visible invariant mass calculated from the position and the energy of the clusters measured in the ECAL has to be greater than 3 GeV.
- The sum of all energy deposits in the ECAL and the HCAL has to be less than 45 GeV in order to reject e^+e^- annihilation events.
- At least 2 tracks must have been found in the tracking chambers. A track is required to have a minimum transverse momentum of 120 MeV/c, at least 20 hits in the central jet chamber, and the innermost hit of the track must be inside a radius of 60 cm with respect to the z axis. The point of closest approach to the origin in the $r\phi$ plane must be less than 20 cm in the z direction and less than 1 cm in the $r\phi$ plane. Tracks with a momentum error larger than the momentum itself are rejected if they have less than 80 hits. The number of measured hits in the jet chamber must be more than half of the number of possible hits, where the number of possible hits is calculated from the polar angle θ of the track, assuming that the track has no curvature.

- The transverse momentum of the event measured in the ECAL and the FD has to be less than 5 GeV/c.
- No track in the event has a momentum greater than 30 GeV/c.
- To remove events with scattered electrons in the FD or in the SW calorimeters, the total energy sum measured in the FD has to be less than 40 GeV and the total energy sum measured in the SW less than 20 GeV. This cut also reduces the contamination from multihadronic e^+e^- annihilation events with their thrust axis close to the beam direction.
- The background due to beam-gas or beam-wall interactions is reduced by the following requirements. The radial distance of the primary vertex from the beam axis has to be less than 3 cm. To estimate the z position of the primary vertex for photon-photon events with typically low multiplicity, we calculate the error-weighted average $\langle z_0 \rangle$ of the z coordinates of all tracks at the point of closest approach to the origin in the $r\phi$ plane. The background due to beam-gas or beam-wall interactions is further reduced by requiring $|\langle z_0 \rangle| < 10$ cm and that the net charge of an event, calculated by adding the charges of all tracks, is less or equal three.

For the remaining events we determine the visible energy $E_{\rm vis}$ and the longitudinal component, $P_{\rm L}$, and the transverse component, $P_{\rm T}$, of the momentum vector of the hadronic final state. These quantities are calculated after a matching algorithm is applied to the data, in order to avoid double-counting of particle momenta. The matching algorithm uses all the information from the ECAL and the HCAL, the FD and the SW calorimeters, as well as from the tracking system. If a calorimeter energy cluster is associated to a track, the cluster energy is compared to the expected energy response $f(\vec{p})$ of the calorimeters for the track with momentum $\vec{p}$. To calculate the energy associated to a track, the pion mass is assumed. The cluster is rejected if the energy of the cluster is less than expected from the track energy. If the cluster energy E exceeds the expected energy by more than what is expected from the resolution, the energy of the cluster is reduced to $E - f(\vec{p})$. In this case the track momentum and the reduced energy of the cluster are taken separately. The output of the matching algorithm is an array of energies and momenta $(E_{\rm h}, \vec{p}_{\rm h})$ which are used to calculate the visible invariant mass $W_{\rm vis}$:

$$W_{\rm vis}^2 = \left(\sum_h E_{\rm h}\right)^2 - \left(\sum_{\rm h} \vec{p}_{\rm h}\right)^2 \quad (2)$$

$$= E_{\rm vis}^2 - P_{\rm L}^2 - P_{\rm T}^2, \quad (3)$$

A cut $|P_{\rm L}/E_{\rm vis}| < 0.85$ is applied, since beam-gas or beam-wall events tend to accumulate at high values of $|P_{\rm L}/E_{\rm vis}|$.

In order to reject events with only leptons in the final state, additional requirements have to be fulfilled for events with $n_{\rm ch} = 2$, where $n_{\rm ch}$ is the number of tracks. Each of the two tracks must have at least 20 $\mathrm{d}E/\mathrm{d}x$ hits in the central jet chamber and the $\mathrm{d}E/\mathrm{d}x$ probability must be smaller than 10% for the electron and for the muon hypothesis. The thrust of the event, calculated in the laboratory system from the output of the matching algorithm, has to be below 0.98.

We use data corresponding to an integrated luminosity of 74.4 pb^{-1} collected with the OPAL detector in the years 1996 and 1997. The integrated luminosity is 9.9 pb^{-1} at $\sqrt{s}_{\rm ee} = 161$ GeV,

10.0 pb^{-1} at $\sqrt{s}_{\rm ee} = 172$ GeV and 54.4 pb^{-1} at $\sqrt{s}_{\rm ee} = 183$ GeV. The error on the luminosity is less than 1%. After applying the above cuts, 23250 events remain at $\sqrt{s}_{\rm ee} = 161$ GeV, 25643 at $\sqrt{s}_{\rm ee} = 172$ GeV and 144147 at $\sqrt{s}_{\rm ee} = 183$ GeV.

5 Monte Carlo simulation

The Monte Carlo generators PYTHIA 5.722 [6] and PHOJET 1.05c [7] are used to simulate photon-photon interactions with Q_1^2 and $Q_2^2 < 4.5$ GeV^2. The photon-photon generator PYTHIA is based on a model by Schuler and Sjöstrand [13] and PHOJET has been developed by Engel [7] based on the Dual Parton model (DPM) [14]. Both generators simulate the process ($e^+e^- \to e^+e^- +$ hadrons) in two stages, firstly $e^+e^- \to e^+e^-\gamma\gamma$ and then $\gamma\gamma \to$ hadrons. The probability of the beam electron emitting a photon is modelled by the Equivalent Photon Approximation (EPA) [15].

Soft processes like quasi-elastic scattering ($\gamma\gamma \to VV$, where V is a vector meson), single-diffractive scattering ($\gamma\gamma \to VX$, where X is a low mass hadronic system) or double-diffractive scattering ($\gamma\gamma \to X_1X_2$) are modelled by both generators. The cross-sections are obtained by fitting a Regge parametrisation to pp, $\overline{\rm p}$p and γp data and by assuming Regge factorisation, i.e. universal couplings of the pomeron to the hadronic fluctuations of the photon. In both generators the quasi-elastic cross-section is about $5-6\%$, the single-diffractive cross-section about $8-12\%$ and the double-diffractive cross-section about $3-4\%$ of $\sigma_{\gamma\gamma}$ for $W > 10$ GeV.

The transition from soft to hard interactions is defined by the transverse momentum of the primary produced partons. For the hard interactions it is assumed that the cross-section can be factorized into parton distribution functions which give the probability to find a parton (quark, gluon) in the photon and matrix elements for the hard subprocess. All possible hard interactions of quarks, gluons and photons are simulated using leading order (LO) matrix elements. As default the SaS-1D parametrisation of the parton distribution functions [16] is used in PYTHIA and the LO GRV parametrisation [17] in PHOJET.

The fragmentation and decay of the parton final state is handled in both generators by the routines of JETSET 7.408 [6]. Initial- and final-state parton radiation is included in the leading logarithm approximation. Both generators include multiple interactions of the remnants of the initial photons.

The two-photon mode of PYTHIA simulates the interactions of real photons with $Q_1^2, Q_2^2 = 0$ GeV^2. The virtuality of the photons, defined by Q^2, enters only through the EPA in the generation of the photon energy spectrum, but the electrons are scattered at zero angle. In PHOJET the Q^2 suppression of the total $\gamma\gamma$ cross-section is parametrised using Generalised Vector Meson Dominance (GVMD). The Q^2 dependence of the quark and gluon densities of the virtual photon and additional Q^2 dependent suppression factors for diffractive[3] processes are also taken into account [7]. The Q^2 dependent transverse momenta of the scattered electrons are also simulated.

All signal and background Monte Carlo samples are generated with full simulation of the

[3]In this paper we refer to the sum of quasi-elastic, single- and double-diffractive events as diffractive events

OPAL detector [18]. They are analysed using the same reconstruction algorithms as are applied to the data. The background from e^+e^- annihilation events $e^+e^- \to (\gamma/Z^0)^* \to q\overline{q}(\gamma)$ is generated with PYTHIA [6]. The leptonic two-photon background processes $e^+e^- \to e^+e^-\tau^+\tau^-$, $e^+e^- \to e^+e^-\mu^+\mu^-$ and $e^+e^- \to e^+e^-e^+e^-$ are simulated with VERMASEREN [19]. The contribution from other background processes is negligible. The Monte Carlo simulated background is less than 1.6% of the total number of selected events . This does not include beam-gas and beam-wall interactions which are estimated to contribute about 2% to the total number of selected events.

Deep-inelastic $e\gamma$ ($= \gamma^*\gamma$) events are generated with HERWIG 5.9 [20]. From the Monte Carlo it is estimated that after all cuts about 1.5% of the remaining events are $e\gamma$ processes with $\max\{Q_1^2, Q_2^2\} > 4.5$ GeV^2 for $\sqrt{s}_{ee} = 183$ GeV. The rate of events where both Q_i^2 are larger than 4.5 GeV^2 is negligible.

6 Unfolding of the hadronic cross-section

In a first step, the differential cross-section $d\sigma_{ee}/dW$ for the process ($e^+e^- \to e^+e^-$ + hadrons) is obtained from the W_{vis} distribution. The measured W_{vis} distribution is shown in Fig. 2 for the data taken at $\sqrt{s}_{ee} = 183$ GeV. The distribution, which falls smoothly over 5 orders of magnitude, is well described by the Monte Carlo simulations which have been normalized to the number of data events after subtracting the Monte Carlo expectation for background and $e\gamma$ events.

The selection efficiency, defined as the ratio of the number N_{sel} of selected Monte Carlo events to the number N_{gen} of generated events at a given generated W, is shown in Fig. 3. It rises from about 10% at $W = 10$ GeV to an almost constant plateau of about 65% for the PHOJET events with $W > 40$ GeV and it decreases again for very high W. The selection efficiency for the PYTHIA events is about 15% lower at $W = 40$ GeV and it approaches the PHOJET selection efficiency at high W. The selection efficiency for diffractive events simulated with PHOJET is much higher than for the diffractive events simulated with PYTHIA.

The relation between W_{vis} and the generated W for all selected PHOJET and PYTHIA Monte Carlo events is shown in Fig. 4. The finite resolution of the W measurement is given by the standard deviations of the W_{vis} distributions in each bin of W which are plotted as vertical bars. The W resolution is consistent for both generators, but differences for the average W_{vis} as a function of the generated W are observed at high W. The main energy losses are caused by hadrons which are emitted at small polar angles θ; they are either lost in the beam pipe, or they are only detected with low efficiency in the electromagnetic calorimeters in the forward regions (FD and SW).

The background determined by the Monte Carlo is first subtracted from the data. Then, the unfolding of the resolution effects, as well as the correction for the detector acceptance and the selection cuts are done with the program GURU [21]. This program for regularised unfolding is based on the Singular Value Decomposition (SVD) method. For systematic checks, the unfolding program RUN [22] has also been used.

The differential cross-sections for the three beam energies, $\mathrm{d}\sigma_{\mathrm{ee}}/\mathrm{d}W$, after unfolding are given in Fig. 5 and Table 1. Bin-to-bin correlations are sizeable, since the chosen bin size is not much larger than the resolution. The size of the correlations also depends on the regularisation procedure of the unfolding. The covariance matrix obtained from the unfolding is given in Table 2.

The differential cross-section $\mathrm{d}\sigma_{\mathrm{ee}}/\mathrm{d}W$ of the process ($\mathrm{e^+e^-} \to \mathrm{e^+e^-} +$ hadrons) can be translated into the cross-section $\sigma_{\gamma\gamma}$ for the process ($\gamma\gamma \to$ hadrons) using the luminosity function $L_{\gamma\gamma}$ for the photon flux [15]. The cross-section for real photons is derived by using form factors $F(Q^2)$ which describe the Q^2 dependence of the hadronic cross-section. In every W bin ΔW_i we determine

$$\sigma_{\gamma\gamma}(W_i') = \int_{\Delta W_i} \frac{\mathrm{d}\sigma_{\mathrm{ee}}}{\mathrm{d}W}\mathrm{d}W \Bigg/ \int_{\Delta W_i} \frac{\mathrm{d}}{\mathrm{d}W}\left(\int \frac{\mathrm{d}^4 L_{\gamma\gamma}}{\mathrm{d}y_1\mathrm{d}Q_1^2\mathrm{d}y_2\mathrm{d}Q_2^2} F(Q_1^2)F(Q_2^2)\mathrm{d}y_1\mathrm{d}Q_1^2\mathrm{d}y_2\mathrm{d}Q_2^2\right)\mathrm{d}W \tag{4}$$

where y_1 and y_2 denote the fraction of the beam energy carried by the photons with $y_1 y_2 \approx W^2/s_{\mathrm{ee}}$ (neglecting Q_1^2 and Q_2^2). The cross-section $\sigma_{\gamma\gamma}$ is given at the bin centre, since the deviation of W_i' from the bin centre due to the finite bin width is found to be small.

The luminosity function $L_{\gamma\gamma}$ and the form factors $F(Q^2)$ for the various W bins are obtained from the program PHOLUM [7] which performs a numerical integration for each W bin over the unmeasured phase space (Q_1^2, Q_2^2 and y ranges). PHOLUM takes into account both transverse and longitudinally polarized photons. The form factors are used in the GVMD approximation of Ref. [23]. The difference between the extrapolation to $Q_1^2 = 0$ and $Q_2^2 = 0$ is about 7% of $\sigma_{\gamma\gamma}$ if the GVMD model is compared to a simple ρ^0 form factor [7]. This uncertainty is not included in the systematic error of the measurement.

In the analysis, the eγ events simulated by HERWIG are subtracted from the data and the photon flux is therefore calculated with a cut on $\max\{Q_1^2, Q_2^2\}$. In order to check this procedure, the analysis was also performed without subtracting the Monte Carlo eγ events. In this case, the photon flux has to be calculated without a cut on $\max\{Q_1^2, Q_2^2\}$. The uncertainty is estimated by comparing these procedures and by using PYTHIA instead of HERWIG for the modelling of the eγ background. The resulting uncertainty on $\sigma_{\gamma\gamma}$ is about 1% and it is therefore neglected.

Assuming the Q_1^2, Q_2^2 and W dependence of the total hadronic cross-section for virtual photons, $\sigma_{\gamma^*\gamma^*}(Q_1^2, Q_2^2, W)$, to factorize, based on a simple GVDM ansatz, the W dependence is preserved when extrapolationg to $\sigma_{\gamma\gamma}(W)$. Although there are some events in the tails towards higher Q_1^2 or Q_2^2 in the $\gamma\gamma$ data of this experiment, extending to several GeV^2, the bulk of the data are at very low Q_1^2 and Q_2^2, so a significant contribution from the tail is unlikely. The medians of the Q_1^2 and Q_2^2 distributions are of the order 10^{-4} GeV^2 (taken from Monte Carlo).

Radiative corrections like multiple photon emission off the incoming electrons are not included in the Monte Carlo generators. They are expected to be small [24] and the effect of the radiative corrections should be much reduced by using the hadronic final state to calculate the kinematics, i.e. the hadronic invariant mass W, of the event.

The three data samples at $\sqrt{s}_{\mathrm{ee}} = 161$, 172 and 183 GeV were independently analysed and the results for the total hadronic two-photon cross-section $\sigma_{\gamma\gamma}$ are found to be in agreement

within 1-2 standard deviations of the statistical error. Furthermore, no systematic trend in the W dependence of $\sigma_{\gamma\gamma}(W)$ is observed as a function $\sqrt{s}_{\rm ee}$. The total cross-sections are therefore averaged using as weight the corresponding integrated luminosities (Tab. 3).

7 Systematic errors

Several distributions of the data are compared to PYTHIA and PHOJET after detector simulation in order to study whether the general description of the data by the Monte Carlo is sufficient to use the Monte Carlo for the unfolding of the cross-section. The Monte Carlo distributions are all normalized to the number of data events after the Monte Carlo expectation for background and eγ events were subtracted from the data. Without this normalisation, using the cross-section predicted by the Monte Carlo generators, the number of selected events is about 10% smaller than in the data for PHOJET and about 10% larger than in the data for PYTHIA.

In both Monte Carlo models about 20% of the cross-section is due to diffractive events in which the final state hadrons go strongly forward or backward into those parts of the detector which have the smallest acceptance. This fraction is almost independent of W for $W > 10$ GeV. The selection efficiency for the diffractive events is small and, although the generated rate is almost the same in both models, different modelling of the diffractive events leads to very different selection efficiencies. For a $W = 70$ GeV only about 6% of all generated diffractive events are selected in PYTHIA, whereas about 20% are selected in PHOJET (Fig. 3). The detector correction therefore has to rely heavily on the Monte Carlo simulation for this class of events.

In order to study the modelling of the diffractive events using the data, we have plotted the maximum rapidity gap $\Delta\eta_{\rm max}$ between the pseudorapidities $\eta = -\ln\tan\theta/2$ of any two particles, neutral or charged, found by the matching algorithm in Fig. 6. Diffractive events are expected to have larger $\Delta\eta_{\rm max}$ due to the colour-singlet exchange [25]. The data are compared to the PHOJET and PYTHIA simulations. Both models underestimate the $\Delta\eta_{\rm max}$ distribution at large $\Delta\eta_{\rm max}$ with PHOJET being closer to the data than PYTHIA. It was checked that the transverse momenta of the scattered electrons, which are simulated in PHOJET but not in PYTHIA, have only a small effect on this distribution.

Significant discrepancies are also found in the distribution of the charged multiplicity $n_{\rm ch}$ (Fig. 7) and the distribution of the thrust variable, T, (Fig. 8). Both Monte Carlo models significantly underestimate the fraction of low-multiplicity events ($n_{\rm ch} < 6$) and overestimate the fraction of high-multiplicity events in comparison to the data and there are also more events with large thrust ($T > 0.925$), in the data. It should be noted that increasing the fraction of diffractive events by factors of two or more in the Monte Carlo does not lead to a significant improvement in these comparisons.

The energy $E_{\rm SW}$ measured in the silicon-tungsten luminometers (SW) is shown in Fig. 9 for all selected events with $E_{\rm SW} > 1$ GeV and the energy $E_{\rm FD}$ measured in the forward detectors (FD) is shown in Fig. 10 for all selected events with $E_{\rm FD} > 2$ GeV. At low $E_{\rm SW}$ both Monte Carlo models lie above the data, but the reasonable agreement of data and Monte Carlo at

large E_{SW} and E_{FD} shows that the remaining background from multihadronic e^+e^- annihilation events and deep-inelastic $e\gamma$ events is small and that this remaining background is reasonably well described by the Monte Carlo. This implies that there are also no events left with an off-momentum beam electron which was scattered upstream hitting SW or FD.

Finally, we plot the ratios $P_{\mathrm{T}}/E_{\mathrm{vis}}$ and $P_{\mathrm{L}}/E_{\mathrm{vis}}$ of the transverse and longitudinal components of the momentum vector of the hadronic system to the visible total energy E_{vis} (Figs. 11,12). Data and Monte Carlo are in good agreement. The small number of events at large $P_{\mathrm{T}}/E_{\mathrm{vis}}$ are expected to be mainly due to background processes. Studies of beam-gas and beam-wall events show that most of these events have $|P_{\mathrm{L}}/E_{\mathrm{vis}}| > 0.85$. The background conditions were different at the three beam energies. In the data taken at $\sqrt{s}_{\mathrm{ee}} = 183$ GeV the beam related background peaked mainly at positive $P_{\mathrm{L}}/E_{\mathrm{vis}} > 0.85$. This explains the small asymmetry in Fig. 12c.

Based on these observations, the following systematic errors are taken into account in the measurement of the cross-sections for every beam energy, separately (Tab. 1):

- In most of the distributions, both Monte Carlo models describe the data equally well and there is no reason for preferring one model over the other for the unfolding of the data. We therefore average the results of the unfolding. The difference between this cross-section and the results obtained by using PYTHIA or PHOJET alone are taken as the systematic error due to the Monte Carlo model dependence of the unfolding.

- An additional error due to the uncertainties of the modelling of the diffractive processes in the Monte Carlo is taken into account. Since there is large uncertainty on the diffractive $\gamma\gamma$ cross-section derived from the HERA measurements [9, 10, 26], we have increased the percentage of diffractive events from 18% to 27% in PHOJET which leads to an increase of $\sigma_{\gamma\gamma}$ by 6%. Increasing the selection efficiency for diffractive events by a factor 2 leads to a decrease of $\sigma_{\gamma\gamma}$ by 6%. These variations of $\pm 6\%$ are used as systematic error.

- The uncertainty in the ECAL energy scale was estimated to be $\pm 3\%$ by comparing the energy distribution reconstructed in the ECAL for e^+e^- annihilation events at $\sqrt{s}_{\mathrm{ee}} = 183$ GeV with the Monte Carlo simulation. ECAL clusters of more than 10 GeV were excluded from this comparison in order to have a distribution of the energy per cluster which is similar to $\gamma\gamma$ events. The systematic error on the total cross-section was then estimated by varying the reconstructed ECAL energy in the Monte Carlo by $\pm 3\%$.

- The electromagnetic calorimeters in the forward direction, SW and FD, are used in the W_{vis} measurement. A possible uncertainty in the energy scale and the detector simulation for hadrons reconstructed in SW or FD was studied by calculating and unfolding W_{vis} without SW and FD information, respectively. The difference between $\sigma_{\gamma\gamma}(W)$ obtained without SW or FD information and $\sigma_{\gamma\gamma}(W)$ obtained with the full detector is taken as the systematic error.

- The trigger efficiency was studied using data samples which were obtained using nearly independent sets of triggers. The trigger efficiency is defined as the ratio of the number of triggered and selected events to the number of selected events. On average, the trigger efficiency for the low W range, $10 < W < 35$ GeV, is greater than 96% and it approaches 100% for larger values of W. Only lower limits on the trigger efficiency can be determined

with this method and therefore no correction factor is applied. However, the lower limit on the trigger efficiency is taken into account as an additional systematic error.

- Studying vertex and net charge distributions, it is estimated that about 2% of the selected events could be due to beam-gas or beam-wall interactions. Hadronic photon-photon events, however, in coincidence with an off-momentum beam electron which was scattered upstream and hitting SW or FD are rejected by the SW and FD energy cuts. The fraction of photon-photon events rejected due to these coincidences is estimated to be less than 2%. Taking into account both effects, a value of 2% is therefore taken as additional systematic error.

- The program GURU [21] has been used for unfolding the $W_{\rm vis}$ distribution. Since the distribution of the charged multiplicity $n_{\rm ch}$ is not well described by the Monte Carlo models, we have studied the influence of this discrepancy by unfolding the two-dimensional $(W_{\rm vis}, n_{\rm ch})$ distribution. No significant difference from the one-dimensional unfolding using GURU is found. The unfolding program RUN [22] can only be used for one-dimensional unfolding. The two unfolding methods implemented in RUN and GURU applied to the $W_{\rm vis}$ distribution also yield consistent results. Therefore no additional systematic error has been taken into account.

- Since the background rate taken from Monte Carlo is only about 1.6%, a possible systematic error is neglected.

- The overall normalisation error due to the uncertainty on the luminosity measurement is less than 1% and is therefore also neglected.

The different systematic errors are summed up in quadrature to obtain the total systematic error. For the total error, the statistical and the total systematic error are added in quadrature. The luminosity-weighted average values of the total cross-section $\sigma_{\gamma\gamma}(W)$ and errors for the different W bins are given in Table 3.

8 Results and model comparisons

The total cross-section for the process $\gamma\gamma \rightarrow$ hadrons, $\sigma_{\gamma\gamma}(W)$, is shown in Fig. 13 in the range $10 \leq W \leq 110$ GeV. In the region $W \leq 20$ GeV, the OPAL measurement is consistent with the results from PLUTO [1], TPC/2γ [2] and PEP/2γ [3] within the large spread and experimental errors of these measurements.

The OPAL measurements exhibit the rise in the W range $10 < W < 110$ GeV which is characteristic for hadronic cross-sections in this energy range. A similar rise was first observed by the L3 experiment [5], but their values of $\sigma_{\gamma\gamma}$ are about 20% lower than the OPAL measurement. L3 used PHOJET only for the unfolding, whereas for the OPAL measurement presented here the unfolding results of PHOJET and PYTHIA are averaged. The OPAL result obtained using only PHOJET is about $5 - 10$% lower than the averaged result.

Several models have been proposed to describe the energy dependence of hadronic cross-sections. One of the interesting questions for hadronic interactions of real photons is whether

they behave the same as hadrons or whether the additional hard contributions to the total cross-sections of photon-induced interactions lead to a faster rise of the total $\gamma\gamma$ and γp cross-sections as a function of energy. Hence we performed a detailed study of the data in the framework of present models.

We study the data within the framework of Regge theory. The total cross-sections for hadron-hadron and photon-proton collisions have been found to be well described [27, 28] by a Regge parametrisation of the form

$$\begin{aligned} \sigma_{\mathrm{AB}} &= X_{1\mathrm{AB}} s^{\epsilon_1} + Y_{1\mathrm{AB}} s^{-\eta_1} + Y_{2\mathrm{AB}} s^{-\eta_2}, \\ \sigma_{\bar{\mathrm{A}}\mathrm{B}} &= X_{1\mathrm{AB}} s^{\epsilon_1} + Y_{1\mathrm{AB}} s^{-\eta_1} - Y_{2\mathrm{AB}} s^{-\eta_2}, \end{aligned} \tag{5}$$

where A and B denote the interacting particles and the centre-of-mass energy squared, s, is taken in units of GeV^2. The first term in the equation is due to soft pomeron exchange and the other terms are due to C-even and C-odd reggeon exchange, respectively [28]. The exponents ϵ_1, η_1 and η_2 are assumed to be universal, whereas the coefficients $X_{1\mathrm{AB}}$ and $Y_{i\mathrm{AB}}$ are process dependent. The values of the exponents were determined in Ref. [28] by a fit to the pp, $\overline{\mathrm{p}}$p, $\pi^{\pm}$p, K$^{\pm}$p, γp and $\gamma\gamma$ total cross-sections:

$$\epsilon_1 = 0.095 \pm 0.002, \qquad \eta_1 = 0.34 \pm 0.02, \quad \text{and} \quad \eta_2 = 0.55 \pm 0.02. \tag{6}$$

The non-zero value of the exponent $\epsilon_1 = 0.095 \pm 0.002$ predicts a slow rise of the total cross-section with energy. The fit in Ref. [28] is dominated by the hadron-hadron data. For γp and $\gamma\gamma$ collisions $Y_2 = 0$, i.e. Eq. 5 reduces to the original form proposed by Donnachie and Landshoff [29]. In this combined fit the available $\gamma\gamma$ data, i.e. not including the OPAL data presented here, were fitted in the range $W > 4$ GeV, yielding $X_{1\gamma\gamma} = (156 \pm 18)$ nb and $Y_{1\gamma\gamma} = (320 \pm 13)$ nb [28].

Assuming factorisation of the pomeron term $X_{1\mathrm{AB}}$, the total $\gamma\gamma$ cross-section can be related to the γp and pp total cross-sections at centre-of-mass energies $\sqrt{s}_{\gamma\gamma} = \sqrt{s}_{\gamma\mathrm{p}} = \sqrt{s}_{\mathrm{pp}}$ larger than about 10 GeV, where the pomeron trajectory should dominate:

$$\sigma_{\gamma\gamma} \simeq \frac{\sigma^2_{\gamma\mathrm{p}}}{\sigma_{\mathrm{pp}}}. \tag{7}$$

Most models for the high-energy behaviour of $\sigma_{\gamma\gamma}$ are based on this factorisation assumption for the soft part of the cross-section. In order to predict $\sigma_{\gamma\gamma}$ via Eq. 7, the fit values of $X_{1\mathrm{pp}}$, $Y_{1\mathrm{pp}}$, $Y_{2\mathrm{pp}}$, $X_{1\gamma\mathrm{p}}$ and $Y_{1\gamma\mathrm{p}}$ are taken from Ref. [28] together with the exponents given in Eq. 6. This simple factorisation ansatz gives a reasonable description of $\sigma_{\gamma\gamma}$, but a faster increase of the cross-section than predicted by $\epsilon_1 = 0.095$ cannot be excluded, as shown in Fig. 13.

The errors on the data points are dominated by systematic errors which are highly correlated. Therefore, the subsequent fits were made using the statistical error, i.e. the covariance matrix given in Tab. 2 and the χ^2 values are only calculated with the statistical errors. If the fits are repeated using the correlation matrix from the unfolding and the total errors, the χ^2 values are reduced by about a factor 400 but the fit results are essentially unchanged. In order to take the correlations due to the systematical errors fully into account, the fits were repeated for each systematic error source, by shifting the values of the cross-sections at each energy by the corresponding amount of the systematic error. The final systematic error on

the fit parameters is then calculated as the square root of the quadratic sum of the differences between the shifted and unshifted fits to the data.

In all subsequent fits to our data, we fix the reggeon term by using the values given in Ref. [28], $\eta_1 = 0.34$, $Y_{1\gamma\gamma} = 320$ nb and $Y_{2\gamma\gamma} = 0$, since we have no data at low W to constrain the fit in this region. We first check the universality of the exponent ϵ_1 by fitting Eq. 5 to the data, leaving the exponent ϵ_1 and the coupling $X_{1\gamma\gamma}$ free. The results of this fit (denoted by fit 1) are given in Table 4 and shown in Fig. 14, together with the OPAL data points. Only the diagonal elements of the covariance matrix from Tab. 2 are shown as error bars. From fit 1 we obtain

$$\epsilon_1 = 0.101 \pm 0.003(\text{stat})^{+0.025}_{-0.020}(\text{sys}) \tag{8}$$

which is in agreement with the value $\epsilon_1 = 0.095 \pm 0.002$ which describes the hadron-hadron and γp data.

In Ref. [8], a scheme is proposed for analysing hadron, real-photon and virtual-photon interactions. This scheme is still based on Regge phenomenology, but introduces an extra term which can be identified with an additional hard pomeron, which has an intercept significantly larger than one. This hard pomeron is assumed to be responsible for the fast rise of the virtual photon-proton γ^*p cross-section. In this model, the cross-section is given by

$$\sigma_{\text{AB}} = X_{1\text{AB}} s^{\epsilon_1} + X_{2\text{AB}} s^{\epsilon_2} + Y_{1\text{AB}} s^{-\eta_1}. \tag{9}$$

In a second fit to our data (denoted by fit 2), we fixed ϵ_1 and η_1 to the values in Eq. 6 and ϵ_2 to the value 0.418 proposed in Ref. [8] to study the significance of the term X_2 in Eq. 9. We obtain

$$X_{2\gamma\gamma} = (0.5 \pm 0.2(\text{stat})^{+1.5}_{-1.0}(\text{sys}))\ \text{nb}. \tag{10}$$

Hence, we find that within the precision of our data this additional term is not required.

Total cross-sections are also described by QCD inspired models. The total cross-sections obtained with some of the models are shown in Fig. 13. All these models predict a steeper rise of $\sigma_{\gamma\gamma}(W)$ than the simple factorisation ansatz based on the pp and γp cross-sections which is not observed within the uncertainty of our data. Schuler and Sjöstrand [13] give a total cross-section for the sum of all possible event classes in their model of $\gamma\gamma$ scattering where the photon has a direct, an anomalous and a Vector Meson Dominance (VMD) component. The direct and anomalous components lead to additional hard interactions which are calculated to leading order in pQCD. Schuler and Sjöstrand consider the spread between this prediction and the simple factorisation ansatz as a conservative estimate of the theoretical band of uncertainty.

We also plot the prediction of Engel and Ranft [7] which is implemented in PHOJET and an eikonalised mini-jet model by Godbole and Panchieri [30] which uses the GRV parton densities of the photon and a transverse momentum cut-off of 2 GeV/c for mini-jet production. The soft part of the cross-section is derived from γp data. Another eikonalized mini-jet model, which assumes simple relations between photon and hadron-induced partonic cross-sections, also predicts cross-sections which are lower by about 20% than the data [31].

9 Conclusion

We presented a measurement of the total hadronic cross-section $\sigma_{\gamma\gamma}(W)$ for the interaction of two real photons, $\gamma\gamma \to$ hadrons, in the range $10 \leq W \leq 110$ GeV for data taken at $\sqrt{s}_{\rm ee} = 161$, 172 and 183 GeV. The cross-section is in good agreement with a simple factorisation ansatz based on γp and pp data.

The energy dependence of the total cross-section has been studied using Regge model parametrisations. We observe the high-energy rise of the total cross-section which is typical for hadronic interactions. We find that previous global fits to the $\sqrt{s}$ dependence of $\sigma_{\rm pp}$, $\sigma_{\gamma{\rm p}}$ and $\sigma_{\gamma\gamma}$ give a good description of our results. The fit of the exponent in the soft pomeron term yields $0.101 \pm 0.003^{+0.025}_{-0.020}$ compared with 0.095 ± 0.002 from the global fit. Within the uncertainty of our measurement, no indication for a faster rise of the $\gamma\gamma$ cross-section than in hadron-hadron or γp interactions is observed.

Further improvements of the description of the hadronic final state by Monte Carlo models are necessary to reduce the systematic error of the measurement. It will also be important to gain a better understanding of the diffractive processes in $\gamma\gamma$ scattering.

Acknowledgements:

We thank R. Engel for many useful discussions and for providing the program PHOLUM.
We particularly wish to thank the SL Division for the efficient operation of the LEP accelerator at all energies and for their continuing close cooperation with our experimental group. We thank our colleagues from CEA, DAPNIA/SPP, CE-Saclay for their efforts over the years on the time-of-flight and trigger systems which we continue to use. In addition to the support staff at our own institutions we are pleased to acknowledge the
Department of Energy, USA,
National Science Foundation, USA,
Particle Physics and Astronomy Research Council, UK,
Natural Sciences and Engineering Research Council, Canada,
Israel Science Foundation, administered by the Israel Academy of Science and Humanities,
Minerva Gesellschaft,
Benoziyo Center for High Energy Physics,
Japanese Ministry of Education, Science and Culture (the Monbusho) and a grant under the Monbusho International Science Research Program,
Japanese Society for the Promotion of Science (JSPS),
German Israeli Bi-national Science Foundation (GIF),
Bundesministerium für Bildung, Wissenschaft, Forschung und Technologie, Germany,
National Research Council of Canada,
Research Corporation, USA,
Hungarian Foundation for Scientific Research, OTKA T-029328, T023793 and OTKA F-023259.

References

[1] PLUTO Collaboration, Ch. Berger et al., Phys. Lett. B149 (1984) 421.

[2] TPC/2γ Collaboration, H. Aihara et al., Phys. Rev. D41 (1990) 2667.

[3] PEP/2γ Collaboration, D. Bintinger et al., Phys. Rev. Lett. 54 (1985) 763.

[4] S.E. Baru et al., Z. Phys. C53 (1992) 219.

[5] L3 Collaboration, M. Acciarri et al., Phys. Lett. B408 (1997) 450.

[6] T. Sjöstrand, Comp. Phys. Comm. 82 (1994) 74;
T. Sjöstrand, LUND University Report, LU-TP-95-20 (1995).

[7] R. Engel and J. Ranft, Phys. Rev. D54 (1996) 4244;
R. Engel, Z. Phys. C66 (1995) 203.

[8] A. Donnachie and P.V. Landshoff, Phys. Lett. B437 (1998) 408.

[9] H1 Collaboration, S. Aid et al., Z. Phys. C69 (1995) 27.

[10] ZEUS Collaboration, J. Breitweg et al., Z. Phys. C75 (1997) 421.

[11] OPAL Collaboration, K. Ahmet et al., Nucl. Instr. and Methods A305 (1991) 275;
P.P. Allport et al., Nucl. Instr. and Methods A346 (1994) 476;
P.P. Allport et al., Nucl. Instr. and Methods A324 (1993) 34.

[12] B.E. Anderson et al., IEEE Transactions on Nuclear Science 41 (1994) 845.

[13] G.A. Schuler and T. Sjöstrand, Z. Phys. C73 (1997) 677.

[14] A. Capella, U. Sukhatme, C.I. Tan and J. Tran Thanh Van, Phys. Rep. 236 (1994) 225.

[15] V. M. Budnev et al., Phys. Rep. 15 (1975) 181-282.

[16] G.A. Schuler and T. Sjöstrand, Z. Phys. C68 (1995) 607.

[17] M. Glück, E. Reya and A. Vogt, Phys. Rev. D46 (1992) 1973;
M. Glück, E. Reya and A. Vogt, Phys. Rev. D45 (1992) 3986.

[18] J. Allison et al., Nucl. Instr. and Methods A317 (1992) 47.

[19] J.A.M. Vermaseren, Nucl. Phys. B229 (1983) 347.

[20] G. Marchesini, B.R. Webber, G. Abbiendi, I.G. Knowles, M.H. Seymour and L. Stanco, Comp. Phys. Comm. 67 (1992) 465.

[21] A. Höcker and V. Kartvelishvili, Nucl. Instr. and Methods A372 (1996) 469.

[22] V. Blobel, DESY-84-118 (1984);
V. Blobel, Proc. 1984 CERN School of Computing, Aiguablava, Spain, CERN 85-09;
V. Blobel, *The RUN manual, Regularized Unfolding for High-Energy Physics Experiments*, program manual, unpublished.

[23] I.F. Ginzburg and V.G. Serbo, Phys. Lett. B109 (1982) 231.

[24] E. Laenen and G.A. Schuler, Phys. Lett. B374 (1996) 217;
I.F. Ginzburg and S.I. Polityko, *Radiative Corrections to Two-Photon Physics. The Experiments "No Tag"*, Preprint TP-No 19 (153), Novosibirsk (1987).

[25] J.D. Bjorken, Phys. Rev. D47 (1993) 101.

[26] A. De Roeck, R. Engel and A. Rostovtsev, *Diffraction in Two-Photon Collisions at TESLA*, hep-ph/9710366.

[27] J.R. Cudell, K.Kang and S.K. Kim, Phys. Lett. B395 (1997) 311.

[28] Review of Particle Physics, Eur. Phys. J. C3 (1998) 205.

[29] A. Donnachie and P.V. Landshoff, Phys. Lett. B296 (1992) 227.

[30] A. Corsetti, R.M. Godbole and G. Panchieri, Phys. Lett. B435 (1998) 441;
M. Drees and R.M. Godbole, Nucl. Phys. B339 (1990);
M. Drees and R.M. Godbole, Z. Phys. C59 (1993);
J.R. Forshaw and J.K. Storrow, Phys. Rev. D46 (1992) 4955.

[31] M.M. Block, E.M. Gregores, F. Halzen and G. Pancheri, *Photon-proton and photon-photon scattering from nucleon-nucleon forward amplitudes*, MADPH-98-1041 and hep-ph/9809403.

W-range [GeV]	$\mathrm{d}\sigma_{\mathrm{ee}}/\mathrm{d}W$ [pb/GeV] $\sqrt{s}_{\mathrm{ee}} = 161$ GeV	$\mathrm{d}\sigma_{\mathrm{ee}}/\mathrm{d}W$ [pb/GeV] $\sqrt{s}_{\mathrm{ee}} = 172$ GeV	$\mathrm{d}\sigma_{\mathrm{ee}}/\mathrm{d}W$ [pb/GeV] $\sqrt{s}_{\mathrm{ee}} = 183$ GeV
10 – 20	$294.0 \pm 3.9^{+31.0}_{-29.9}$	$319.4 \pm 3.9^{+33.8}_{-31.9}$	$320.6 \pm 1.7^{+32.5}_{-29.9}$
20 – 35	$89.0 \pm 1.3^{+\ 8.9}_{-\ 8.8}$	$96.1 \pm 1.3^{+10.3}_{-10.3}$	$104.4 \pm 0.6^{+11.3}_{-11.2}$
35 – 55	$33.5 \pm 0.6^{+\ 3.2}_{-\ 3.1}$	$36.4 \pm 0.6^{+\ 3.5}_{-\ 3.3}$	$39.4 \pm 0.3^{+\ 4.0}_{-\ 3.9}$
55 – 80	$11.2 \pm 0.2^{+\ 1.4}_{-\ 1.1}$	$13.9 \pm 0.3^{+\ 1.4}_{-\ 1.1}$	$14.8 \pm 0.1^{+\ 1.5}_{-\ 1.4}$
80 –110	$3.5 \pm 0.1^{+\ 0.7}_{-\ 0.5}$	$4.8 \pm 0.1^{+\ 1.0}_{-\ 0.7}$	$5.3 \pm 0.1^{+\ 0.8}_{-\ 0.6}$

Table 1: The differential cross-section $\mathrm{d}\sigma_{\mathrm{ee}}/\mathrm{d}W$ at $\sqrt{s}_{\mathrm{ee}} = 161$, 172 and 183 GeV for the anti-tagged two-photon events. The first error is statistical and the second systematic.

W-range [GeV]	10 - 20	20 - 35	35 - 55	55 - 80	80 -110
10 - 20	3.37	0.90	-1.43	-1.23	0.42
20 - 35	0.90	4.36	1.98	-1.89	-2.84
35 - 55	-1.43	1.98	6.86	5.04	-3.10
55 - 80	-1.23	-1.89	5.04	13.43	10.21
80 - 110	0.42	-2.84	-3.10	10.21	27.44

Table 2: The covariance matrix of the statistical errors on $\sigma_{\gamma\gamma}(W)$ obtained from the unfolding. The units are nb^2.

W-range [GeV]	10 – 20	20 – 35	35 – 55	55 – 80	80 – 110
$\sigma_{\gamma\gamma}$ [nb]	362	372	414	439	464
stat. error	± 2	± 2	± 3	± 4	± 5
MC model	±21	±30	±29	±29	±53
diffraction	±22	±22	±25	±26	±28
ECAL	±16	± 9	± 9	±10	±14
no FD	− 1	− 9	− 5	+13	+41
no SW	− 4	+ 2	+ 7	+10	+11
trigger	+14	+ 9	+ 8	+ 7	+ 5
beam-gas	± 7	± 7	± 8	± 9	± 9
total syst.	$^{+37}_{-35}$	$^{+40}_{-40}$	$^{+42}_{-41}$	$^{+45}_{-41}$	$^{+75}_{-62}$
total error	$^{+38}_{-35}$	$^{+40}_{-40}$	$^{+42}_{-41}$	$^{+45}_{-41}$	$^{+75}_{-62}$

Table 3: The total hadronic two-photon cross-section $\sigma_{\gamma\gamma}$ and the contributions from the various systematic errors (in nb)

	$X_{1\gamma\gamma}$ [nb]	ϵ_1	$X_{2\gamma\gamma}$ [nb]	ϵ_2	$Y_{1\gamma\gamma}$ [nb]	η	χ^2/ndf
fit 1	$180 \pm 4^{+30}_{-32}$	$0.101 \pm 0.003^{+0.025}_{-0.020}$	0		320	0.34	137/3
fit 2	$182 \pm 2^{+22}_{-22}$	0.095	$0.5 \pm 0.2^{+1.5}_{-1.0}$	0.418	320	0.34	130/3
PDG [28]	156 ± 18	0.095 ± 0.002	0		320 ± 130	0.34 ± 0.02	

Table 4: Results of the various fits of Regge type parametrisations to the total $\gamma\gamma$ cross-section. If no error is given, the parameter was fixed in the fit. The values of χ^2 per number of degrees of freedom (ndf) are calculated based on the covariance matrix of the statistical errors. The results are compared with the OPAL data in Fig. 14. For details see text.

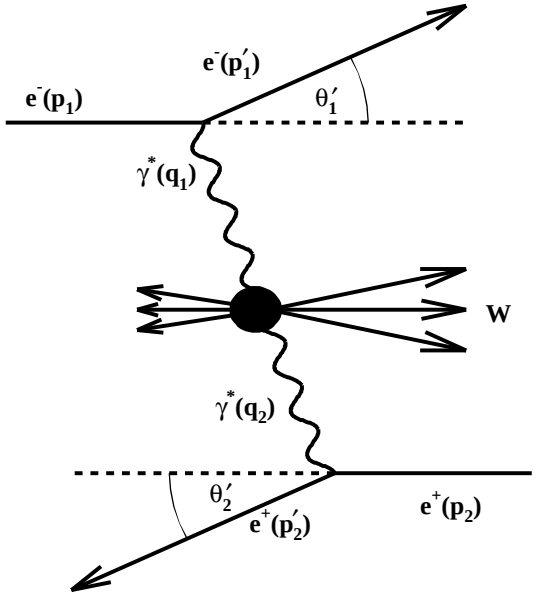

Figure 1: Diagram of a photon-photon scattering process

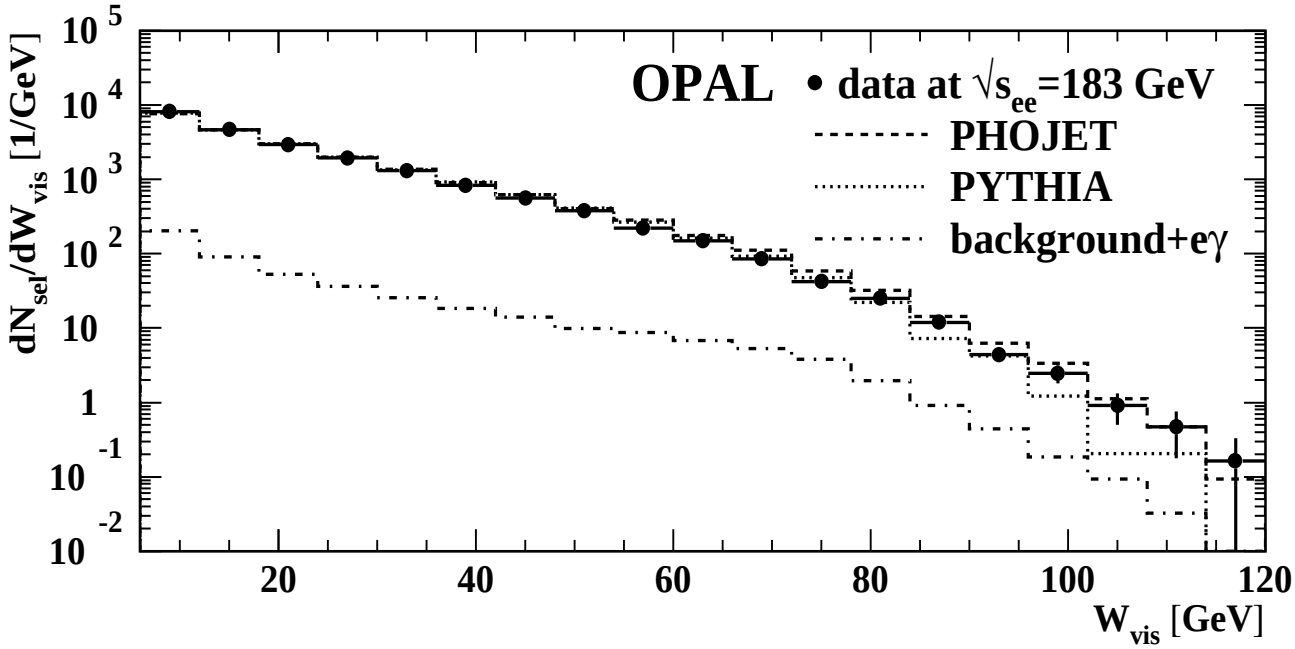

Figure 2: The $W_{\rm vis}$ distribution for all selected events at $\sqrt{s}_{\rm ee} = 183$ GeV with $W_{\rm vis} > 6$ GeV after background subtraction. The data are compared to PHOJET (dashed line) and PYTHIA (dotted line). Only statistical errors are shown. The Monte Carlo background and eγ events which have been subtracted from the data are shown as the dashed-dotted histogram.

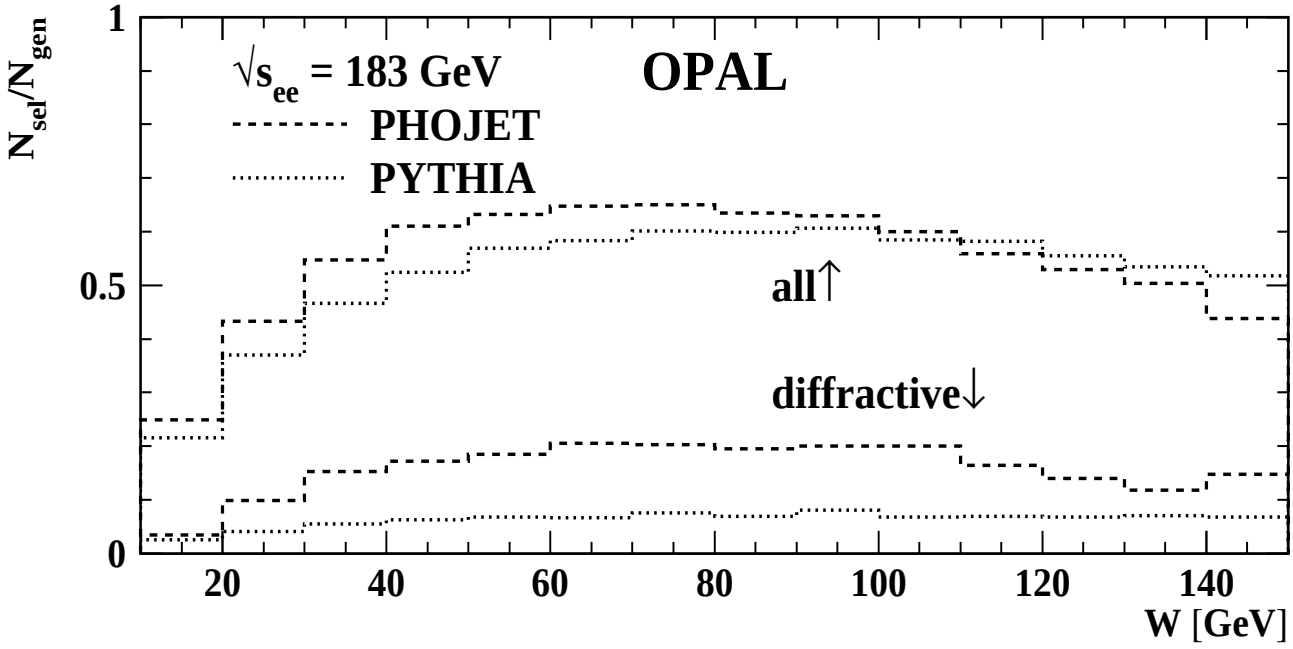

Figure 3: The selection efficiency defined by the ratio of the number of selected events, $N_{\rm sel}$, to the number of generated events, $N_{\rm gen}$, at a given generated invariant mass W for PHOJET (dashed line) and PYTHIA (dotted line) at $\sqrt{s}_{\rm ee} = 183$ GeV. The lower curves give this ratio for the sum of the diffractive events separately.

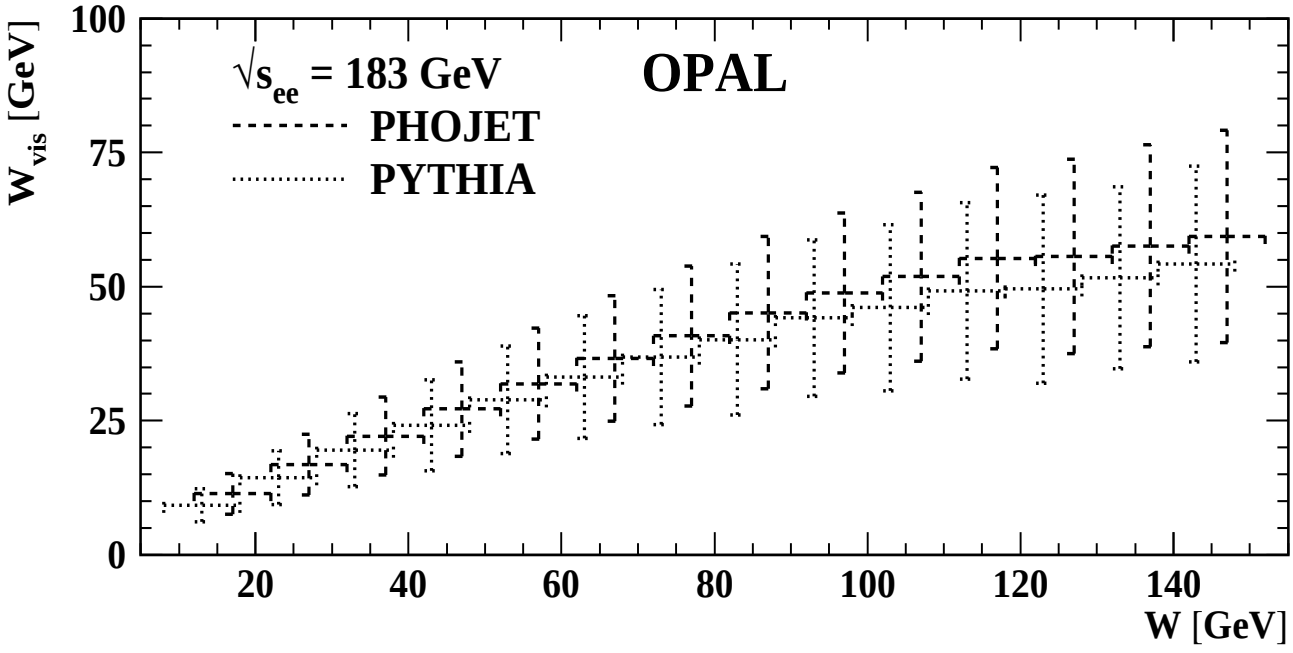

Figure 4: The relation between the visible hadronic invariant mass $W_{\rm vis}$ and the generated W for all selected PHOJET (dashed) and PYTHIA (dotted) Monte Carlo events at $\sqrt{s}_{\rm ee} = 183$ GeV. The vertical bars show the standard deviation (spread) of the $W_{\rm vis}$ distribution in each bin.

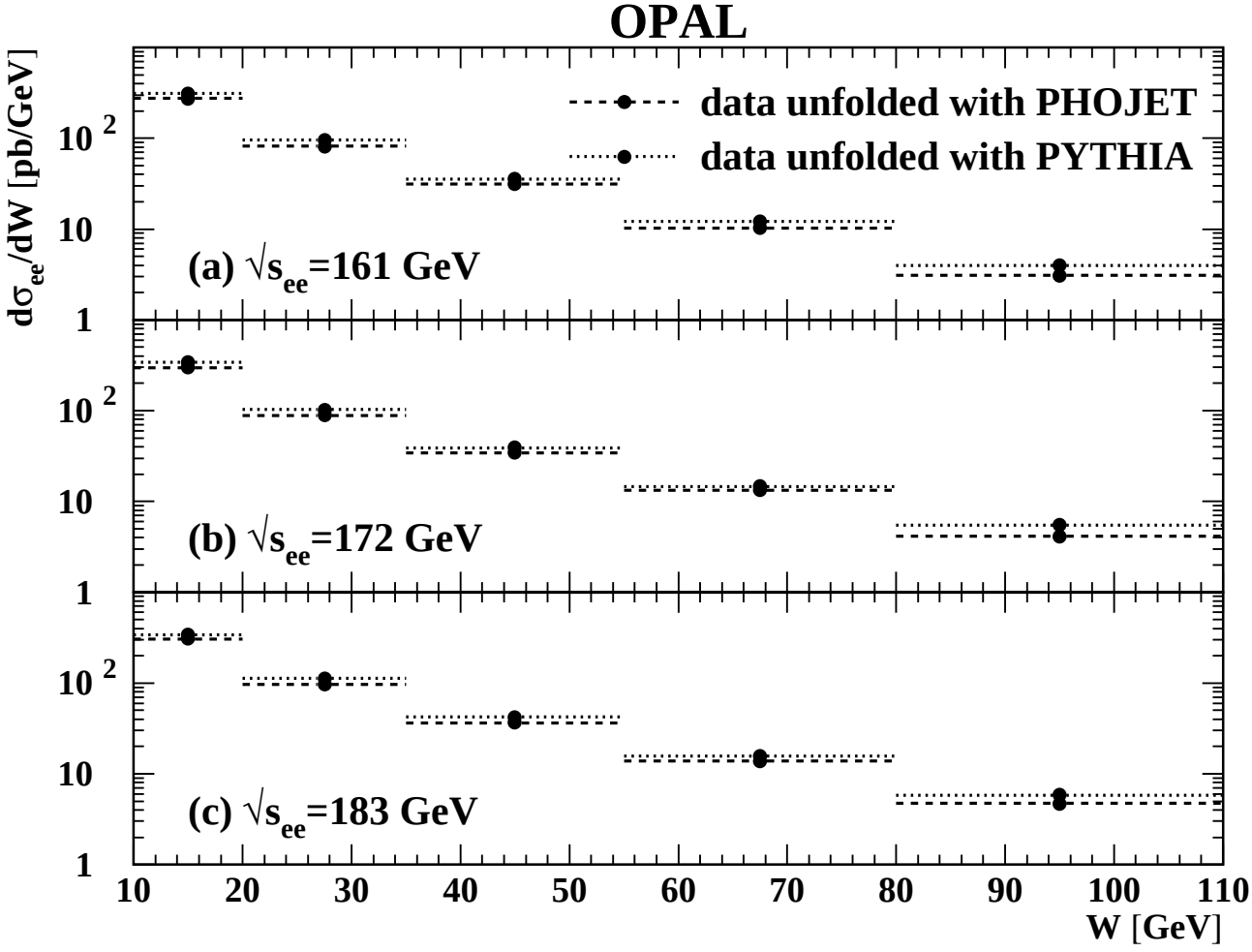

Figure 5: The differential cross-section $\mathrm{d}\sigma_{\mathrm{ee}}/\mathrm{d}W$ at (a) $\sqrt{s}_{\mathrm{ee}} = 161$ GeV, (b) $\sqrt{s}_{\mathrm{ee}} = 172$ GeV and (c) $\sqrt{s}_{\mathrm{ee}} = 183$ GeV for the anti-tagged two-photon events. Unfolding and acceptance corrections were done with PHOJET (dashed line) and with PYTHIA (dotted line). The statistical errors are smaller than the symbol size.

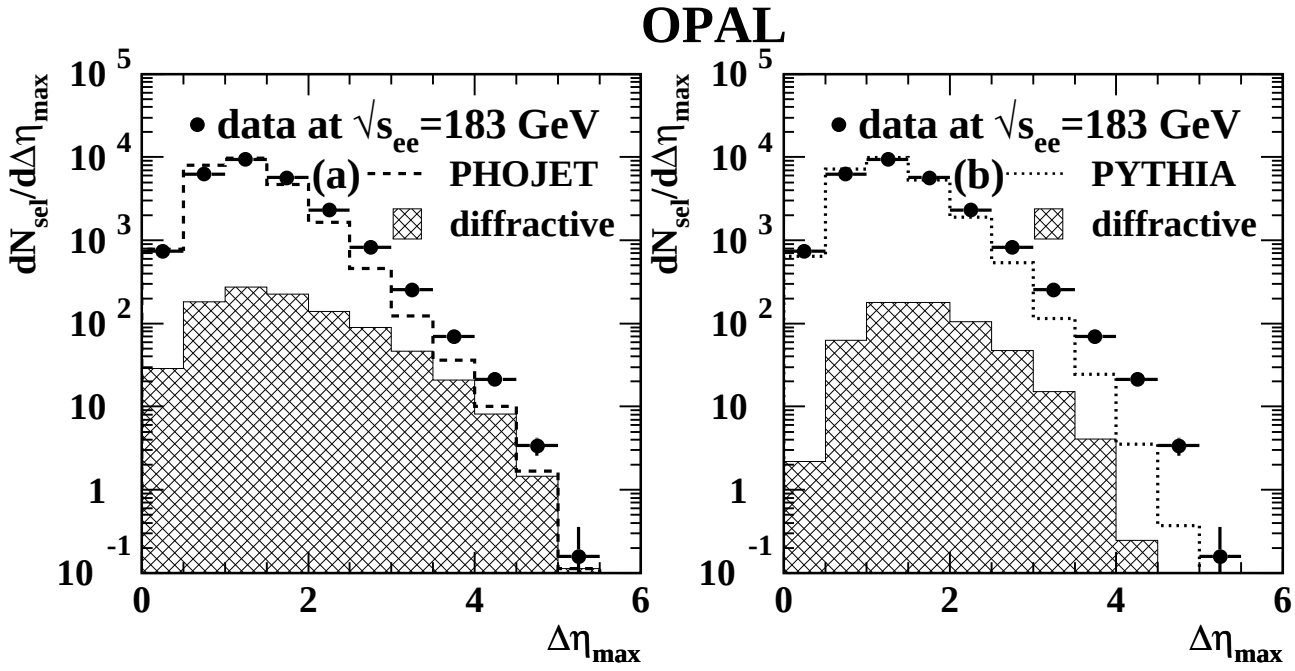

Figure 6: The $\Delta\eta_{\max}$ distribution for all selected events at $\sqrt{s}_{\rm ee} = 183$ GeV with $W_{\rm vis} > 6$ GeV after subtracting the Monte Carlo background and eγ events. The $\Delta\eta_{\max}$ distribution is compared to the full a) PHOJET and b) PYTHIA simulation. The diffractive component is shown separately. Only statistical errors are shown.

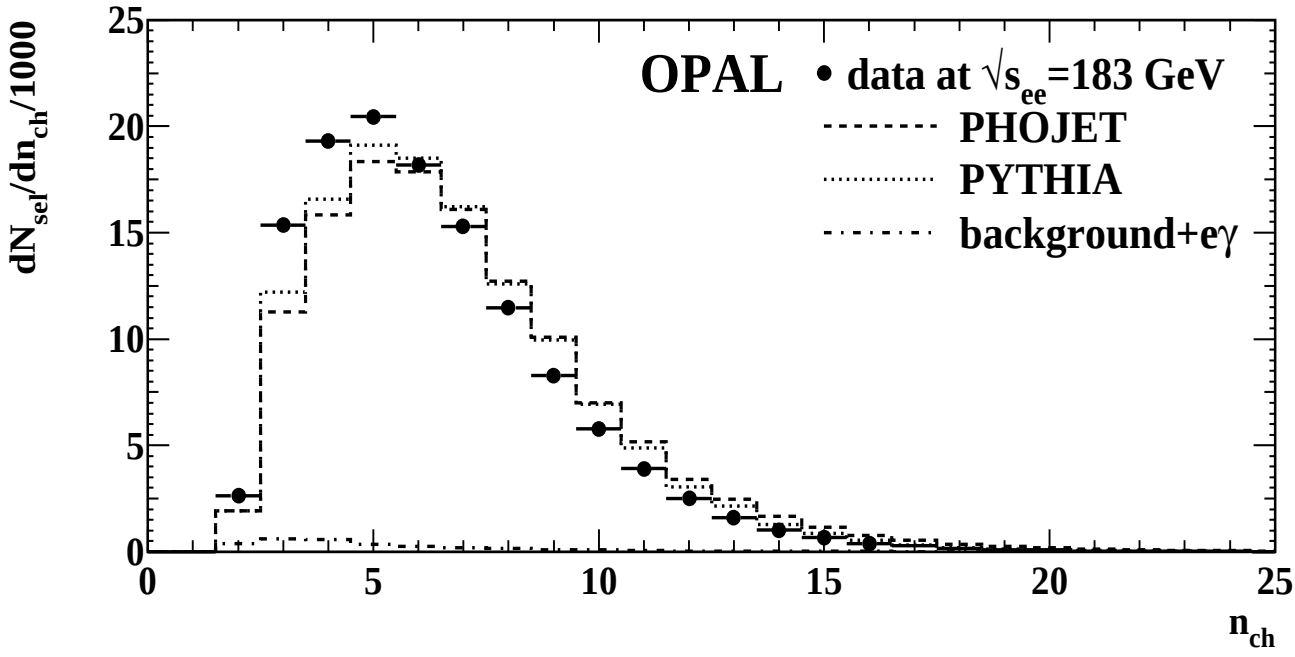

Figure 7: The distribution of the charged multiplicity $n_{\rm ch}$ for all selected events at $\sqrt{s}_{\rm ee} = 183$ GeV with $W_{\rm vis} > 6$ GeV compared to PHOJET (dashed line) and PYTHIA (dotted line). The statistical errors are smaller than the symbol size. The subtracted Monte Carlo background and eγ events are shown as the dashed-dotted histogram.

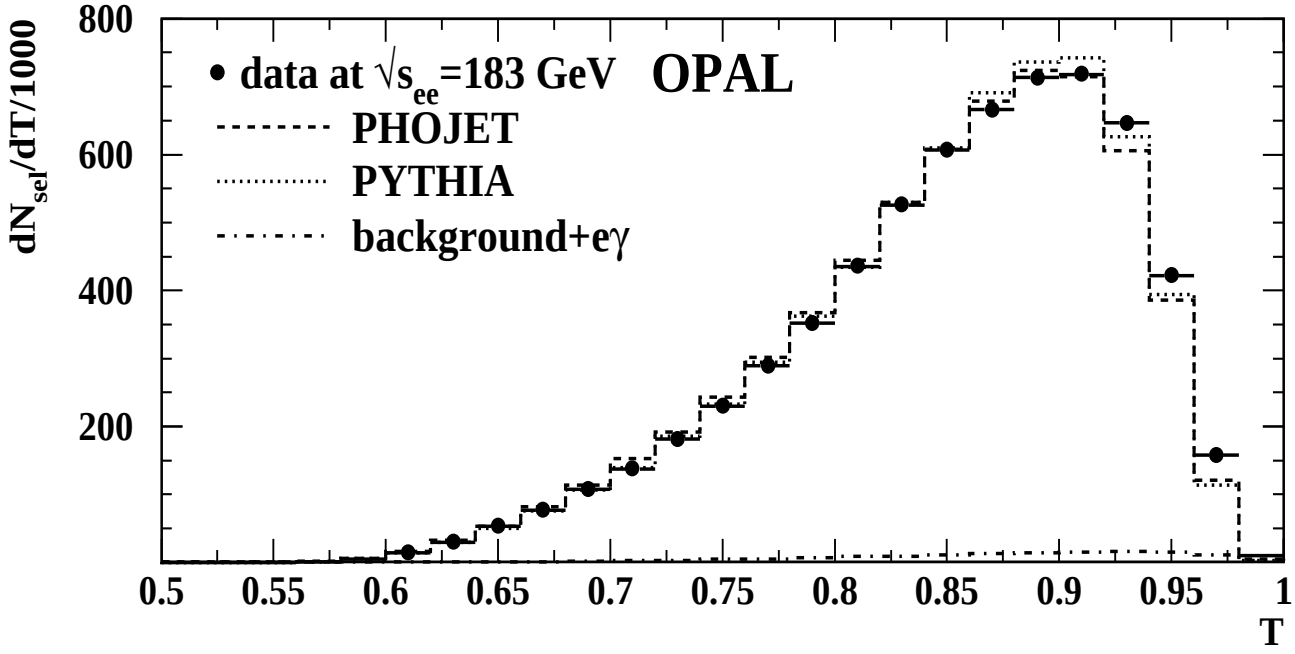

Figure 8: The distribution of the thrust T for all selected events at $\sqrt{s}_{\rm ee} = 183$ GeV with $W_{\rm vis} > 6$ GeV compared to PHOJET (dashed line) and PYTHIA (dotted line). The statistical errors are smaller than the symbol size. The subtracted Monte Carlo background and eγ events are shown as the dashed-dotted histogram.

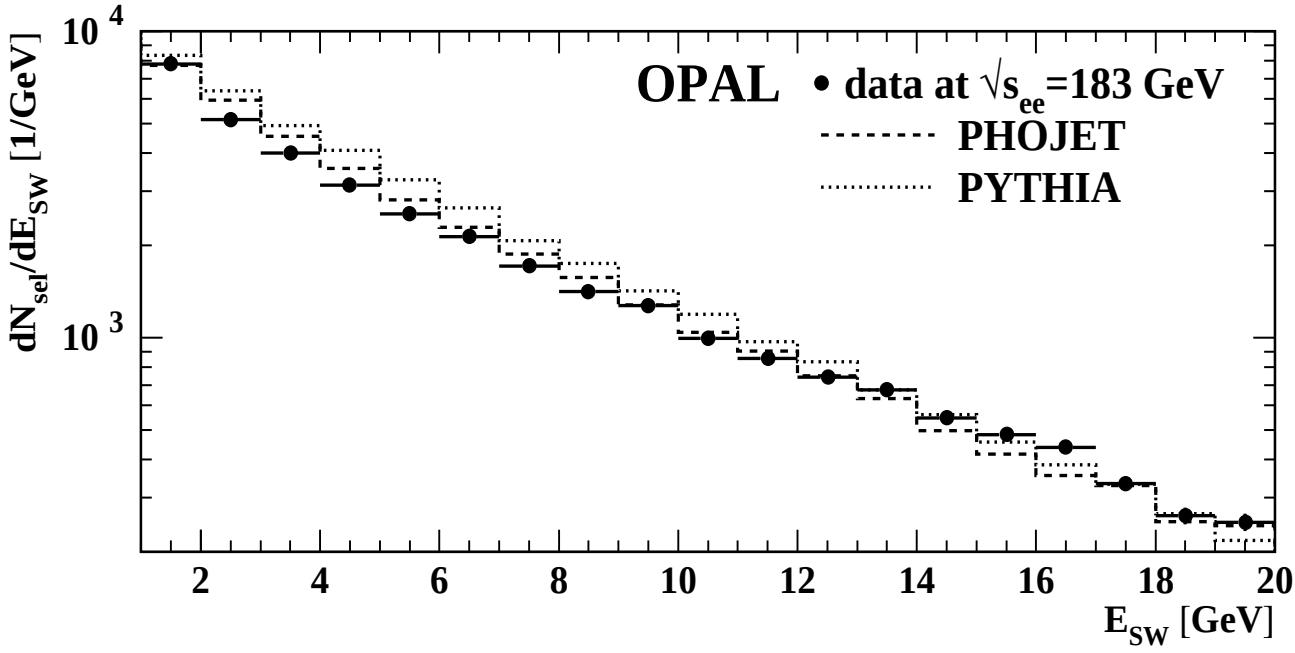

Figure 9: The distribution of the energy $E_{\rm SW}$ for all selected events at $\sqrt{s}_{\rm ee} = 183$ GeV with $W_{\rm vis} > 6$ GeV and $E_{\rm SW} > 1$ GeV compared to PHOJET (dashed line) and PYTHIA (dotted line). The statistical errors are smaller than the symbol size. Due to the chosen scale the subtracted Monte Carlo background and eγ events are not visible.

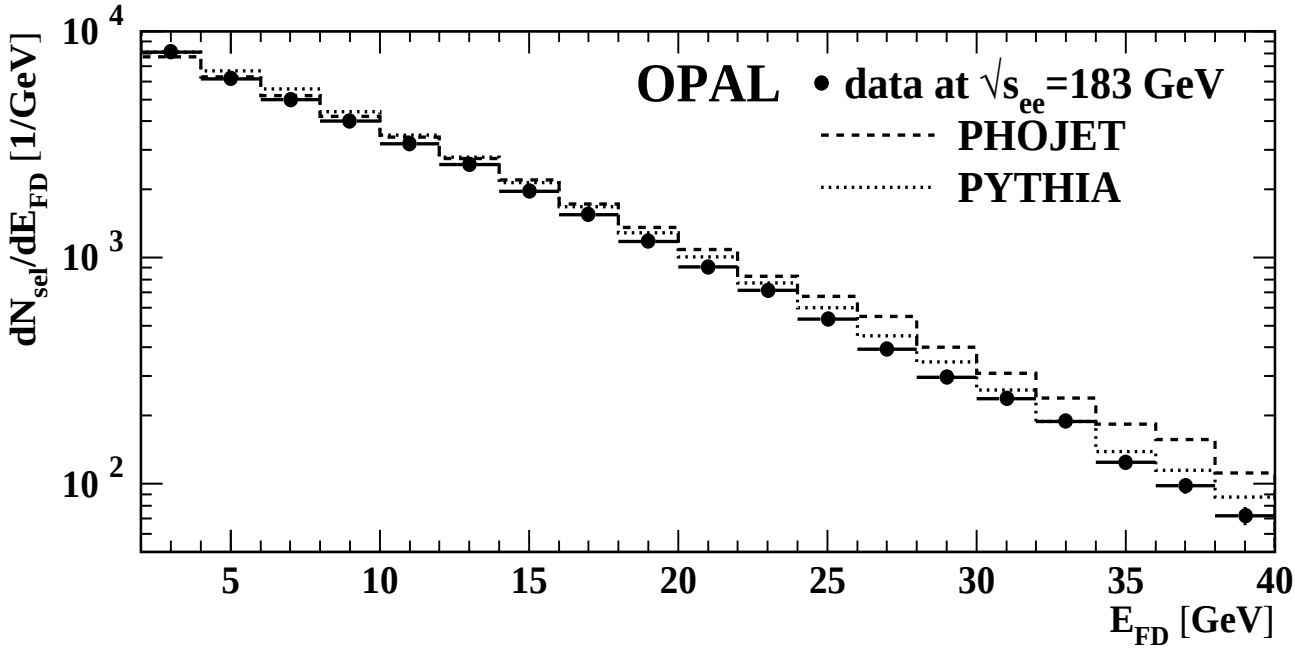

Figure 10: The distribution of the energy $E_{\rm FD}$ for all selected events at $\sqrt{s}_{\rm ee} = 183$ GeV with $W_{\rm vis} > 6$ GeV and $E_{\rm FD} > 2$ GeV compared to PHOJET (dashed line) and PYTHIA (dotted line). The statistical errors are smaller than the symbol size. Due to the chosen scale the subtracted Monte Carlo background and eγ events are not visible.

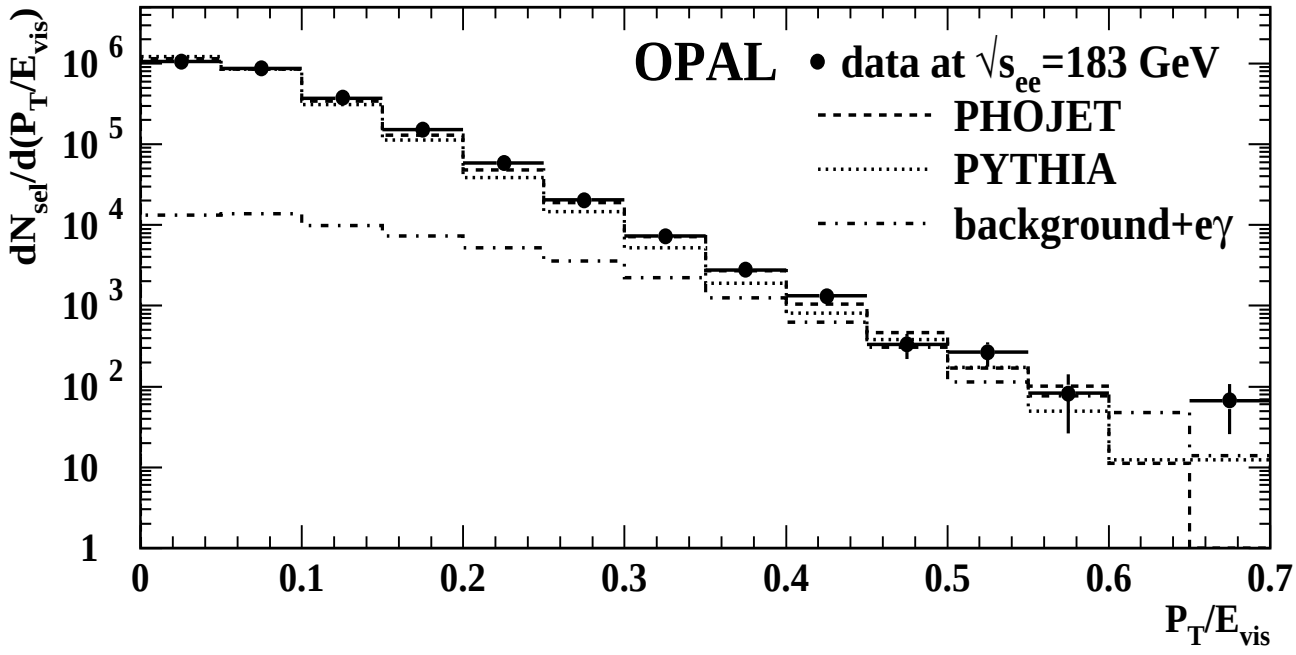

Figure 11: The distribution of the ratio $P_{\rm T}/E_{\rm vis}$ for all selected events at $\sqrt{s}_{\rm ee} = 183$ GeV with $W_{\rm vis} > 6$ GeV compared to PHOJET (dashed line) and PYTHIA (dotted line). Only statistical errors are shown. The subtracted Monte Carlo background and eγ events are shown as the dashed-dotted histogram.

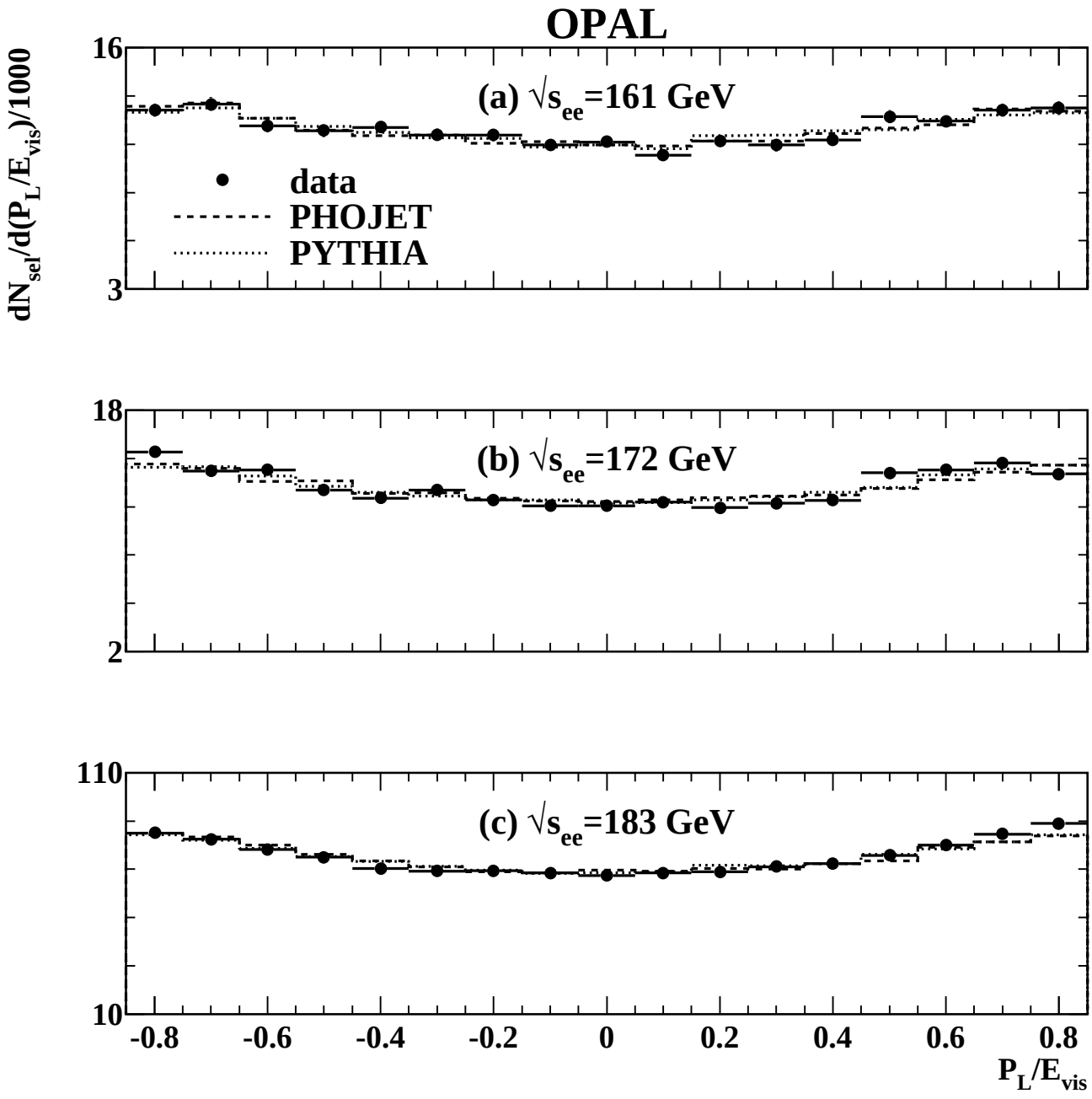

Figure 12: The distribution of the ratio $P_{\mathrm{L}}/E_{\mathrm{vis}}$ for all selected events at $\sqrt{s}_{\mathrm{ee}} = 161, 172$ and 183 GeV with $W_{\mathrm{vis}} > 6$ GeV compared to PHOJET (dashed line) and PYTHIA (dotted line). The statistical errors are smaller than the symbol size. Due to the chosen scale the subtracted Monte Carlo background and eγ events are not visible.

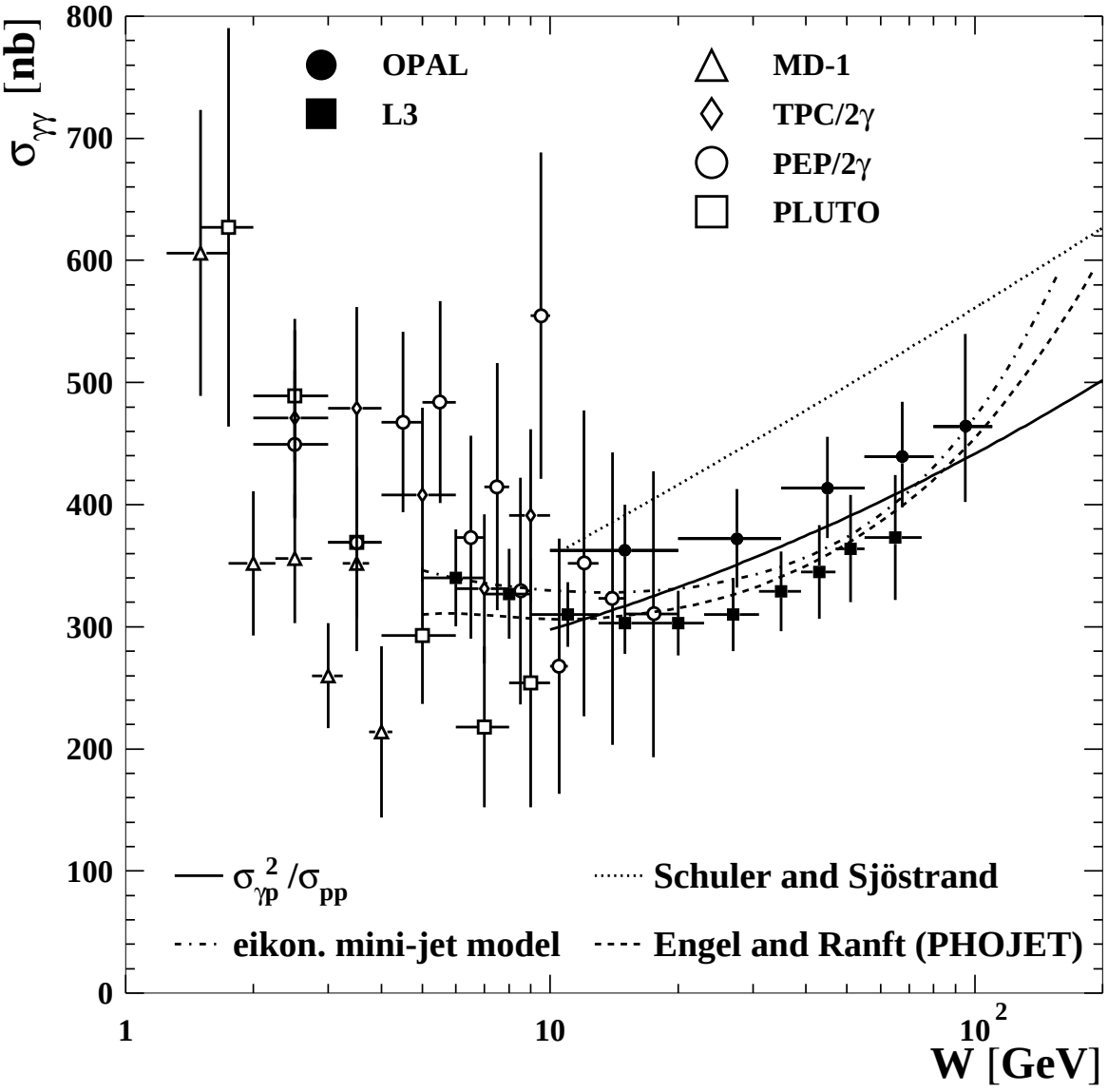

Figure 13: The total cross-section $\sigma_{\gamma\gamma}(W)$ for the process $\gamma\gamma \rightarrow$ hadrons. The OPAL measurement is compared to measurements by PLUTO [1], TPC/2γ [2], PEP/2γ [3], MD1 [4] and L3 [5]. The statistical and the systematic errors are added in quadrature. The normalisation uncertainty of 7% due to the extrapolation to $Q_1^2, Q_2^2 = 0$ GeV^2 is not included. The data are compared to a simple factorisation ansatz based on a Donnachie-Landshoff fit to total cross-sections [29] (solid line). The dashed-dotted line is the eikonalised mini-jet model by Godbole and Panchieri [30], the dotted line is the model of Schuler and Sjöstrand [13] and the dashed line is the model of Engel and Ranft [7].

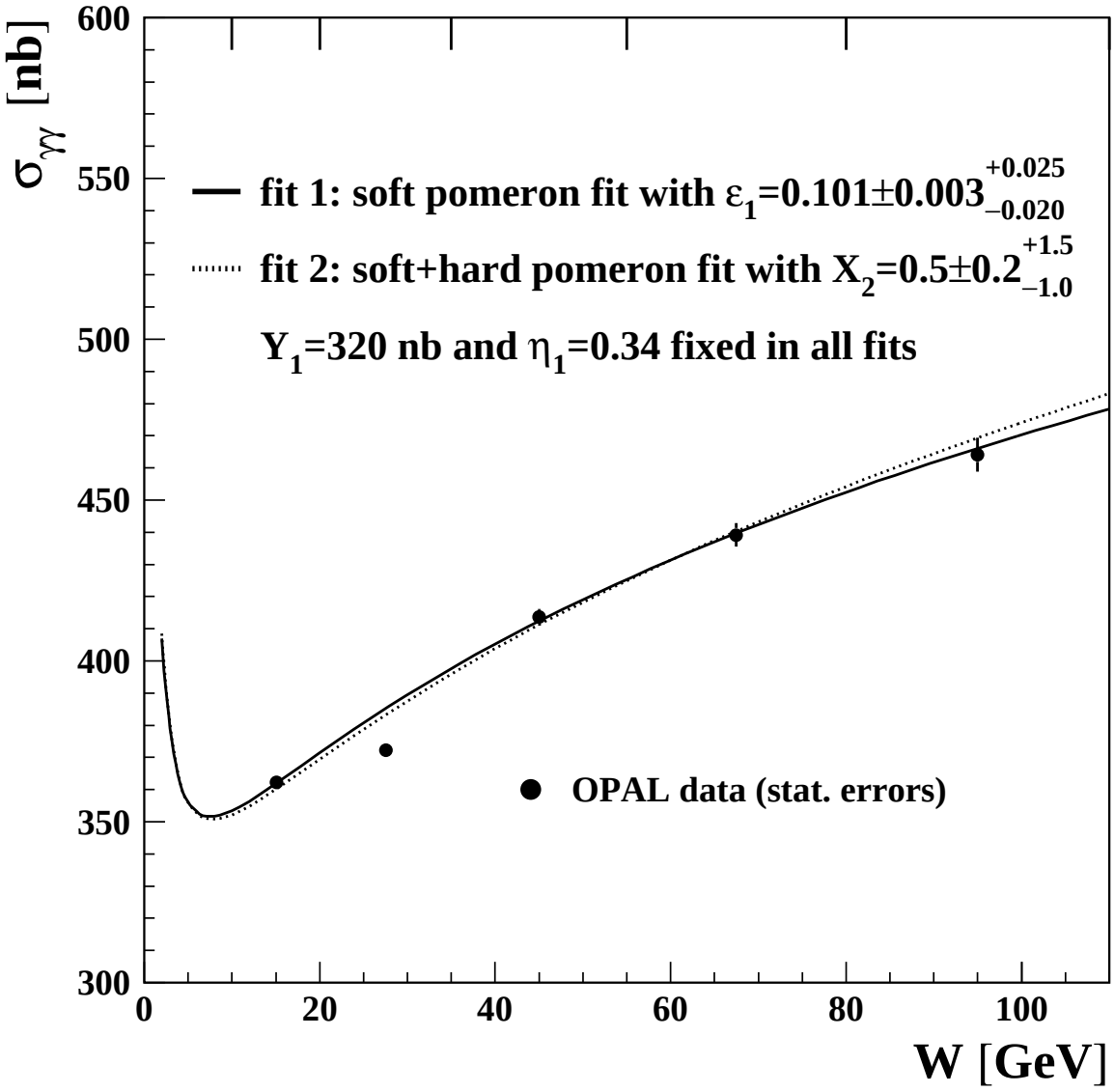

Figure 14: The total cross-section $\sigma_{\gamma\gamma}(W)$ for the process $\gamma\gamma \rightarrow$ hadrons. Different Regge parametrisations have been fitted to the OPAL data. Only the statistical errors are shown. The vertical lines at the top of the figure delineate the bin boundaries.